UNIVERSITY OF OKLAHOMA

GRADUATE COLLEGE

60°S-62°S Witnessed a Shift Pattern of Southern Ocean Boundary Layer Aerosols and CCN

A THESIS

SUBMITTED TO THE GRADUATE FACULTY

in partial fulfillment of the requirements for the

Degree of

MASTER OF SCIENCE IN METEOROLOGY

By

QING NIU
Norman, Oklahoma
2021

60°S-62°S Witnessed a Shift Pattern of Southern Ocean Boundary Layer Aerosols and CCN

A THESIS APPROVED FOR THE
SCHOOL OF METEOROLOGY

BY THE COMMITTEE CONSISTING OF

Dr. Greg McFarquhar, Chair

Dr. Roger Marchand

Dr. Steven Cavallo

Dedication

To my beloved grandma, she never understands why I pursue a degree across the Pacific Ocean, but she always respects my choice...

Acknowledgments

I would like to thank Dr. Greg McFarquhar and the School of Meteorology at the University of Oklahoma for providing the opportunity to attend Graduate School and their continued guidance and support resulting in this work. I would also like to thank the Department of Energy for funding this research and the Atmospheric Radiation Measurement science community for providing the data used in this study. I also appreciate all the instructions from my committee members.

Table of Contents

List of Figures

Abstract

The Southern Ocean (SO), dominated by high surface wind speeds associated with frequent cyclones, is the most pristine environment on Earth, providing a natural laboratory to study the correlation of marine boundary layer aerosols with meteorological conditions in order to enhance the understanding of processes responsible for aerosol formation and loss. The Atmospheric Radiation Measurement Program's Mobile Facility-2 (AMF2) onboard the Australian icebreaker Aurora Australis (AA) obtained ship-based cloud, precipitation and aerosol measurements during the 2017-18 Measurements of Aerosols, Radiation and CloUds over the SO (MARCUS) Experiment during cruises across the SO. A novel machine-learning algorithm was developed and implemented to remove time periods when aerosol measurements were contaminated by the ship stack. The algorithm identified patterns of simultaneously decreasing ozone caused by titration of NO_x near the stack outlet and increasing carbon monoxide caused by insufficient diesel combustion as contaminated periods. Compared to a statistically based algorithm that used aerosol measurements as input, this algorithm retained 31% more uncontaminated data, enabling a more comprehensive analysis of SO background aerosol characteristics.

The concentrations of condensation nuclei (CN) in the accumulation mode with aerosol diameters (D) between 70 and 1000 nm measured by an Ultra-High-Sensitivity Aerosol Spectrometer (UHSAS) were found to be well correlated with the concentrations of Cloud Condensation Nuclei (CCN) at 0.2% supersaturation ($R^2 = 0.691$). Comparisons between aerosols measured between 50°S and 60°S with those measured south of 62°S were conducted. Though aerosol number concentration in both regions was dominated by aerosols with D $<$100 nm, differences significant at the 0.05 level were noted, including the mean aerosol concentrations with 700 nm $<$D $<$1000 nm were 47% less south of 62°S compared to between 50°S and 60°S, while those with 100 nm $<$D $<$350 nm were 32% higher.

Aerosol hygroscopicity growth factor (GF) which provides indirect chemical composition information, was measured as the ratio of wet aerosol diameter at 80% relative humidity to the dry diameter. Between 50°S and 60°S, it has modes of 1.30, 1.38, 1.49 and 1.67 for particles with 50, 100, 200, 250 nm dry diameter respectively, while south of 60°S, the modes are 1.41, 1.42, 1.34 and 1.34 respectively. Aerosol scattering Angstrom Exponents (α) measured at wavelength 450, 550 and 700 nm, which provide information about aerosol size and dominant mode have modes of 0.5 ($\alpha_{450-550}$), 0.8 ($\alpha_{450-700}$) and 1.0 ($\alpha_{550-700}$) between 50°S and 60°S, and 1.1 ($\alpha_{450-550}$), 1.4 ($\alpha_{450-700}$) and 1.5 ($\alpha_{550-700}$) south of 60°S. The higher GF for aerosol with D >200 nm between 50°S and 60°S is consistent with higher sea salt ratio noted in related previous literature, suggesting the influence by surface wind speed on bubbles breaking out. The lower GF for aerosol with D <100 nm is consistent with higher fraction of organic mass in aerosols as noted in previous literature, potentially caused by the wind-driven injection of organic aggregates that accumulate in surface ocean waters. The relative stable GF value for aerosols with 50 nm <D <250 nm south of 60°S might be caused by larger contribution from sulfate and methane sulfonic acid, with sources as gas to particle formation and cloud processing etc. Overall, the latitude range between 50°S and 60°S has lower α with higher total aerosol scattering coefficient and stronger size-dependent hygroscopicity GF than the latitude range south of 60°S, which suggested the larger aerosol effective radius, higher aerosol loading and size-dependent aerosol chemical composition.

To further understand reasons for differences in aerosol properties south of 62°S, air mass origins were determined using the Hysplit4 back trajectory model. This analysis showed aerosols between 50°S and 60°S originated from westerly flow near the boundary layer, whereas those south of 62°S originated in the free troposphere over the Antarctic continent.

The impact of wind speed on aerosol measurements is consistent with the production of sea spray aerosols over the boundary layer between 50°S and 60°S as the CCN at

0.2% supersaturation were significantly positively correlated with horizontal wind speed, weaker positively correlated with overall wind speed but negatively correlated with wind speed less than 10 $m\ s^{-1}$ south of 62°S. This may be caused by the change of size distribution since aerosols with D <350 nm is significantly negatively correlated to horizontal wind speed while aerosols with D >350 nm is significantly positively correlated to horizontal wind speed.

Chapter 1

Introduction

The Southern Ocean (SO), surrounding the ice-covered Antarctic continent and sea ice, is the most pristine environment on Earth due to its remoteness from anthropogenic and continental aerosol sources (Hoose et al. 2009; Hamilton et al. 2014; McCoy et al. 2015; Uetake et al. 2020). Extratropical cyclones are pervasive over the SO (Simmonds and Keay 2000; Hoskins and Hodges 2005; Lang et al. 2018) and are accompanied by high surface winds (Yuan et al. 2009), substantial low cloud cover (below 3 km altitude), and boundary layer precipitation (Mace 2010; IPCC 2013; McCoy et al. 2014). In recent years, an increasing number of field campaigns have been conducted to explore both clouds and aerosol processes over the SO due its unique remote and synoptically active environment (Schmale et al. 2019; McFarquhar et al. 2021).

There is a large bias of shortwave radiation reflected by the cold sectors of extratropical cyclones over the SO in climate models (Naud et al. 2014; Bodas-Salcedo et al. 2014, 2016) compared to observed radiative fluxes, indicating that persistent low clouds, their supercooled water concentrations and albedo are poorly represented in models (Flato et al. 2013; Bodas-Salcedo et al. 2014). The microphysical properties of low clouds, such as the concentration of droplets, influence cloud reflectance and are sensitive to the concentrations of Cloud Condensation Nuclei (CCN). Therefore understanding the sources and sinks of CCN is crucial. Over the remote SO in the Marine Boundary Layer (MBL), natural aerosols, especially those in the accumulation mode (aerosols with diameter (D) between 70 nm and 1000 nm), have long residence times of approximately 5 days in the free troposphere at altitudes between 4 and 8 km because they do not sediment quickly nor coagulate easily (Williams et al. 2002). They are thus capable of serving as CCN as they are large

enough to nucleate when supersaturation in the atmosphere exceeds the critical supersaturation for their nucleation.

Because the concentration of CCN is influenced by both the size and composition of aerosols, the sources and sinks of marine boundary layer aerosols must be identified to understand CCN concentrations over the SO. Hanley et al. (2010) showed that sea spray aerosols constituting sea salt and primary organic aerosol are dominant over the SO and are generated by wind-wave interactions. The formation of secondary aerosols near the surface from biogenic gaseous emissions and gas to particle conversion is another key process, especially during summer when the SO is one of the most biologically active regions in the world (Ayers and Gras 1991; O'Dowd et al. 1997; Simó and Dachs 2002; McCoy et al. 2015; Fossum et al. 2018; Alroe et al. 2020). Chen et al. (2018) pointed out that this gas to particle conversion occurs mostly through dimethyl sulfide (DMS) to methanesulfonic acid (MSA) MSA or sulfur dioxide vapor to sulfuric acid. These two CCN types are referred hereafter as SS-CCN (Sea Spray CCN) and MB-CCN (Marine Biogenic CCN), respectively. Entrainment of free tropospheric homogeneous nucleated new particles into the Southern Hemisphere marine boundary layer produce boundary layer Aitken mode aerosols, which can serve as CCN near the surface (Quinn et al. 2017). Humphries et al. (2015) find that ultra-fine particles, generally defined as particles with D $<$100 nm, over the SO are linked to airmasses arriving from the Antarctic as new particle formation and growth events occur over both the sea ice marginal zone in the boundary layer and free troposphere over the Antarctic plateau (Lachlan-Cope et al. 2020). Wet removal is regarded as the dominant sink of CCN and accumulation mode aerosols, which occurs when a cloud droplet forms in supersaturated conditions (Pruppacher and Klett 1997). These scavenged aerosols can fall out and reach the ground after raindrops form through collision-coalescence.

The relative contributions of these different aerosol sources and sinks over the SO can vary as a function of environmental conditions. One key environmental factor is wind speed that affects the concentration of MBL aerosols and the CCN (Latham and Smith 1990;

Murphy et al. 1998). To investigate the relationship between aerosols and wind speed, lab experiments have manually produced sea spray aerosol (SSA) via the bursting of bubbles on the crests of waves for wind speeds larger than 10 $m\ s^{-1}$ (Massel 2007; O'Dowd and de Leeuw 2007). However, these experiments can only quantify SSA emission fluxes as a function of wind speed for specific types or sizes of aerosols (Barthel et al. 2018), and such relations might not apply universally. The chemical composition of marine aerosols as a function of location and environmental conditions over the SO is poorly known. Thus, knowledge about the source of accumulation mode aerosols, which primarily serve as CCN, is especially needed as a function of location and meteorological conditions, to understand the properties of clouds over the SO.

Particulate hygroscopicity can be used as an indirect indicator of the particle chemical composition (Svenningsson et al. 2006; Schill et al. 2015). The first aerosol hygroscopicity and chemical measurements made in Antarctica to characterise the coastal Antarctic aerosol features in summer season were conducted in 2007 at Aboa station. Xu et al. (2020) quantitatively pointed out sub-micron aerosols with chemical compositions of mainly sulphuric acid, partly neutralised by ammonia, together with MSA and other organics are hygroscopic, implying they can serve as CCN. To compliment these observations made only at an Antarctic station, the current study focuses on variations of hygroscopicity as a function of latitude, in order to identify potential aerosol sources and chemical composition. Other aerosol properties, such as total aerosol scattering coefficient (Bs) and Angstrom Exponent (AE) that have been intensively studied by Graßl and Ritter (2019); Barman et al. (2019) for investigating aerosol loading and aerosol type classification, can also be beneficial for understanding CCN active aerosol over the SO.

Humphries et al. (2021) examined how the latitudinal gradient of CCN concentration was impacted by the latitudinal distribution of horizontal wind speed and scavenging by combining ship-borne aerosol data acquired during the Clouds, Aerosols, Precipitation, Radiation, and atmospherIc Composition Over the southeRn oceaN (CAPRICORN) field

campaign with analysis of the Hysplit simulated total precipitation rate within the past 120 hours along a back trajectory from where the data were acquired. The CCN concentration had a strong inverse dependence on precipitation, whereas high wind speeds directly contributed to higher CCN concentrations.

Simmons et al. (2021) examined aerosol and meteorological data taken over the East Antarctic, especially those obtained over the coastal seasonal ice zone during the Polar Cell Aerosol Nucleation (PCAN) campaign, conducted using the ship R/V Investigator during the 2017 summer (January–March). Aerosols measured south of 56.5°S are classified first with current wind direction and then absolute humidity. Based on the Hysplit model that established the source region of the measured aerosols, the drastic increase of aerosols with $D > 3$ nm was linked to the SE wind and to the origin from either the free troposphere or Antarctic continent. They also showed that, north of 56.5°S aerosols had different modal sizes, and there was larger absolute humidity and lower CCN concentrations compared to observations further south in the seasonal ice zone.

The study presented here extends the Humphries et al. (2021) and Simmons et al. (2021) studies by examining in more detail how the concentration in different aerosol size ranges and aerosol properties, (ie., hygroscopicity and AE) vary with latitude, wind speed and history of precipitation over the SO. This detailed analyse allows testing of hypotheses on how the role of different physical processes associated with variations in the meteorological patterns such as wind speed, sea ice and air mass origin impact the physical properties of accumulation mode aerosols and CCN, and how these vary with latitude.

To conduct these investigations, it is necessary to use the aerosol data that represent ambient conditions over the SO. In this study, data from the field campaign Measurements of Aerosols, Radiation and CloUds over the SO (MARCUS) in 2017-2018 Australia summer are used. The observations were acquired by instruments installed on the icebreaker Aurora Australis (AA), which transversed back and forth over the Australasian SO between Hobart, Australia and the Australian East Antarctic stations. A common problem

with using ship-borne aerosol observations is potential contamination from the chimney on the ship. Ship-stack exhaust is a source of CCN that has been previously observed to increase the concentration of cloud droplets while reducing their sizes (Coakley et al. 1987). Humphries et al. (2021) developed a statistical algorithm to remove periods contaminated by ship-stack exhaust using CAPRICORN data acquired aboard the RV Investigator. However, one algorithm input, the total aerosol concentration, is one of the aerosol variables used in subsequent analysis. This can make it difficult to separate natural aerosol variation from contamination. Furthermore, when this algorithm was applied to the MARCUS data together with manual screening with data as black carbon and ozone by Humphries et al. (2021), only 11% of data were not contaminated. In this study, a novel machine learning algorithm is designed to automatically identify time periods using CO and O_3 when ship stack contamination occurs without using aerosol data as input and is shown to retain a greater fraction of the original data than the Humphries et al. (2021) algorithm.

The remainder of the study is organized as follows. Chapter 2 introduces the machine learning algorithm used to eliminate periods of ship-stack contamination. Chapter 3 presents observations of accumulation mode aerosols and CCN separated according to whether data were collected north or south of 60°S. Chapter 4 explores the meteorological controls of this observed latitudinal dependence. Chapter 5 summarizes the main findings and offers directions for future research.

Chapter 2

Instrumentation and Data

This chapter contains three sections, first provides an overview of the field campaign which provides the data for this study. It then describes the instruments used for observations during the campaign. The other text in this chapter introduces the data pre-processing steps and customized quality control which enables the following scientific discussion about natural aerosols over the SO in Chapter 3 and Chapter 4.

2.1 Voyage overview

During MARCUS, the icebreaker Aurora Australis made three full latitudinal transects of the SO (Fig. 2.1) on resupply voyages from Hobart, Australia (42.9° S, 147.3° E) to the Australian Antarctic station: Casey (66.16 S, 110.3 E), Davis (68.3° S, 77.6°E), and Mawson (67.4°S, 62.5°E) and also made one voyage to Macquarie Island (54.4°S, 158.5°E) from 29th October, 2017 to 24th March, 2018. This 144-day period included the Austral spring, summer and part of fall. This seasonal coverage, combined with the nature of the resupply voyages meaning specific cloud or weather systems were not targeted, means that a climatologically representative set of data on the aerosol, cloud and precipitation properties over the SO were obtained. The transit time across the SO and through the sea ice from Hobart to the Antarctica were approximately two weeks, with the AA spending approximately one week moored at a station during the resupply. Aerosol probes are not used in this study while the AA was in port for those times to avoid anthropogenic pollutants from the Antarctic stations influencing the data. McFarquhar et al. (2021) provides more details on the meteorological systems sampled during MARCUS and the context of the MARCUS data in terms of other projects conducted over a similar time period in the SO.

Fig. 2.1 shows the ship tracks for the whole MARCUS campaign colored by voyage. Along three of the four voyages, there shows up sea ice near the Antarctic coast based on the sea ice scale in the view acquired from the sea state monitor on-board. More details about sea ice is discussed in Chapter 4.3.

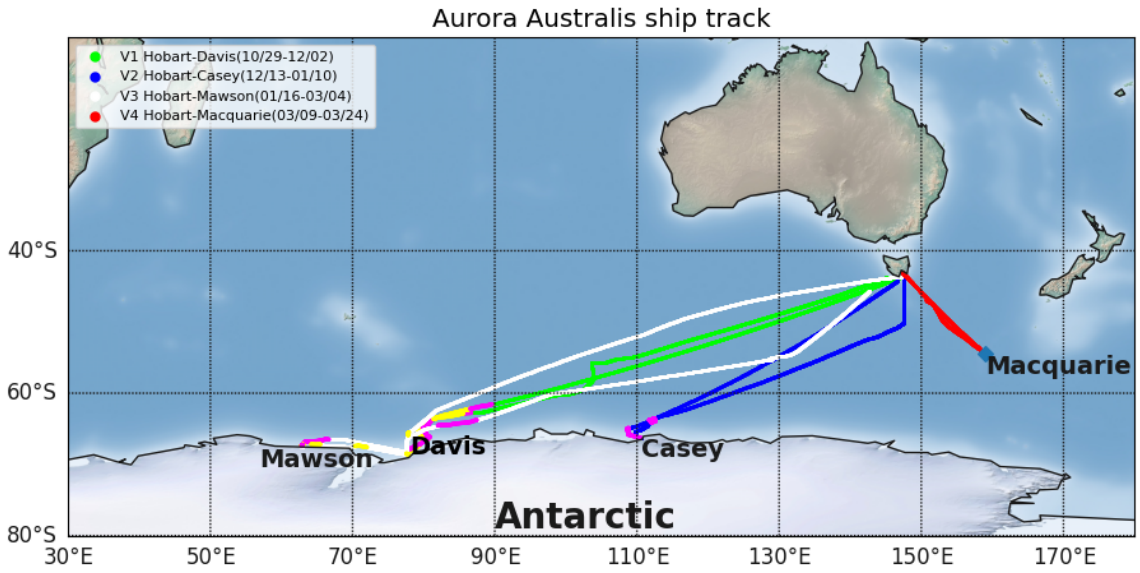

Figure 2.1: Ship tracks during MARCUS by voyage with color shown by legend. Pink color along the tracks represent the floating scattered sea ice in the view and yellow color near the Antarctic coast represent the time with fully-covered sea ice.

2.2 Instrumentation

McFarquhar et al. (2021) gives an overview of all the instrumentation installed on the AA to measure cloud, aerosol, radiative and precipitation properties during MARCUS. In this section, the instrumentation and processing procedures are provided for all data used in this study.

All instruments are divided into two categories, aerosol associated measurements are described in Table 2.1 and measurements of ship motion and meteorological conditions are provided in Table. 2.2 .

2.2.1 Aerosol Instruments

The primary measurements of aerosol were acquired with instruments included in the second ARM Mobile Facility 2 (AMF2) Aerosol Observing System(AOS) ((Uin et al. 2019), (J and Smith 2020)). The AMF2 AOS includes a suite of instruments in a container that was located at the top of a wheelhouse (approximately 24 m above sea level) on the bridge deck of the AA. The AOS inlet was covered by a stainless steel rain shield with a meteorological station mounted on top. The exact location of the instruments on the Autora Australis can be found in the Appendix of Humphries et al. (2021).

The Ultra-High Sensitive Aerosol Spectrometer (UHSAS) manufactured by Droplet Measurement Technologies, Inc. in the AMF2 AOS provides aerosol size distributions by counting the particle number concentrations in a number of size bins with diameters between 60 and 1000 nm with a time resolution of every 10 seconds. The light scattered by particles passing through an infrared laser (1054 nm) is measured by optical detectors to determine particle size. Output data were recorded after every sample. The first five bins from the UHSAS (D $<$70 nm) are not used in this research since the data are not of high quality according to the ARM instrument translator. The UHSAS had a stable sample flow of around 50 $cm^{-3}\ min^{-1}$ during MARCUS, indicating concentrations in the range of 0 to 3600 cm^{-3} could be detected. The manufacturer specifies the uncertainty of particle sizing as within 2.5% of particle size (Uin 2016d).

The TSI Model 3772 Condensation Particle Counter (CPC) manufactured by TSI Inc. Shoreview was used to detect particles down to 10 nm but smaller than 10 μm at an aerosol flow rate of 1.0 $L\ min^{-1}$, over a concentration range from 0 to 10^4 particles cm^{-3}. It condenses and grow particles to super-micron sizes and then count them individually with an Optical Particle Counter (OPC). Unlike the measurement made at a static site where uncertainty are dominant by statistical error in single particle-counting mode, in the field, the inlet flow rate typically has variability of up to 5%, primarily contributing to the measurement uncertainty (Kuang 2016a,b).

The Cloud Condensation Nuclei Counter (CCN) manufactured by Droplet Measurement Technologies Inc. measures the concentration of particles that act as CCN as a function of supersaturation in the humidifier. The CCN-100 draws a volume of air into one column chamber with an adjustable supersaturation, where an OPC is used to size and count the particles at several values of supersaturation. For MARCUS, the supersaturation (SS) cycles through 0.1%, 0.2%, 0.5%, 0.8% and 1.0%, every 10 minutes with 2 minutes required for a transition between SS. The whole cycle normally lasts for one hour and therefore provides the concentration of CCN at each SS hourly. Uncertainty of single particle counting depends on the total aerosol particle concentration and is within 4% (Uin 2016b).

The Humidified Tandem Differential Mobility Analyzer (HTDMA) 3100 manufactured by Brechtel Manufacturing, Inc. measures aerosol particle growth factor due to water uptake. The first differential mobility analyzer (DMA) selects a narrow size range of dry aerosol particles (For MARCUS, every 50 nm steps from 50 to 250 nm), these particles are then exposed to 80% RH. The second DMA along with a CPC are used to measure the resulting size distribution. From the initial dry particle size and the size distribution of the humidified particles, a growth factor is derived. Particle sizing uncertainty is approximately 4%, according to the manufacturer and instrument handbook (Uin 2016a).

The TSI model 3563 Integrating Nephelometer instrument is an instrument that measures aerosol light scattering, main measurements include the aerosol particle optical scattering coefficients (total scatter and backscatter) in unit of m^{-1} for three wavelengths (700, 550, and 450 nm). Based on modelling and experimental results the systematic uncertainty is within 10% (Uin 2016c).

2.2.2 Meteorological Measurements

Other instruments provided measurements including trace gas concentrations, meteorological parameters, ship motions, and vertical thermodynamic profiles of the boundary layer

Table 2.1 Aerosol Measurement during the MARCUS used in this study

Measurements	Symbol	Unit	Instruments	Acronym	Time resolution	Associated publication
Total aerosol number concentration	CN	cm^{-3}	Condensation Particle Counter, Model 3772, TSI Inc., Shoreview, MN	CPC	1s	Brechtel, FJ, and SM, Kreidenweis, 2000a, b
Aerosol number size distribution from 70 nm to 1um	$dN/dlnD_P$	$cm^{-3}nm^{-1}$	Ultra-High Sensitivity Aerosol Spectrometer, DMT, Boulder, CO	UHSAS	10s	Hermann, M et al. 2007
CCN number concentration at five supersaturation (SS)	$N_{ccn,ss}$	cm^{-3}	Cloud Condensation Nuclei counter, Model CCN-100, DMT, Boulder, CO	CCN	Each SS level for 12 min	Roberts, GC, and Nenes, A. 2005
Aerosol scattering coefficient	B_S	Mm^{-1}	Nephelometer, Model 3563, TSI Inc., Shoreview, MN	Nephelometer	5s, inlet upper cut size changes between 1um and 10um every hour	Anderson, TL and JA Ogren. 1998.
Hygroscopicity Growth Factor	GF	/	Humidified Tandem Differential Mobility Analyzer, Model 3100, Brechtel Inc., Hayward, CA	HTDMA	Each size distribution for 5 min	Xerxes F. et al., 2014

and free troposphere. These includes the Los Gatos Research (LGR) $CO/H_2O/N_2O$ analyzer instruments (CO-ANALYZERs), an Ozone monitor and AOSmet (Aerosol Observing System for meteorology) that are also part of the AMF2 AOS. Table 2.2 provides a list of these measurements used in this study during the MARCUS.

Table 2.2 Meteorological Measurements during the MARCUS used in this study

Measurements	Symbol	Unit	Instruments	Time resolution
Ship location and altitude	lat, lon, height	degree, meter	iXSea Global Positioning System (GPS)-aided Inertial Navigation System(INS)	< 0.001s
CO mixing ratio	CO	ppmv	CO/H2O/N2O Gas Analyzer, Model 48C, Thermo Electron Cor. Franklin, MA	1s
Ozone concentration	O_3	ppb	Ozone monitor, Model 49i, Thermo Electron Cor. Franklin, MA	1s
Meteorological parameters: Wind speed and direction, precipitation rate etc.	/	degree and ms^{-1} relative to the ship	AMF2 Aerosol Observing System (AOSmet doi.org/10.5439/1025153.)	1s
Sea ice scale	/	/	Camera for Sea state Monitor	/

CO-ANALYZERs provide the molar fraction of CO by measuring the absorption of infrared radiation at 4.6 μm. Similarly, the model 49i O_3 analyzer manufactured by the Thermo Fisher Scientific, Inc. measures the molar fraction of O_3 by measuring light absorbance at 254 nm.

AOSmet includes meteorological measurements of ambient relative humidity, and ship-relative wind speed and direction (oriented to the bow of the ship). It also contains a Vaisala weather transmitter (WXT520) mounted on top of the AOS aerosol inlet, at a height of approximately 34 meters above the sea surface (Kyrouac 2019). This wind information will be used as input data for wind correction in Section 2.3.4.

The iXSea Global Positioning System (GPS)-aided Inertial Navigation System(INS) reads high-accuracy ship motion data in three translational frames and three rotational frames of reference, as well as the ship's current position (latitude and longitude) and its attitude (roll, pitch, and yaw angles). These parameters of ship motion are required to correct the measured winds from the AOSmet whose wind speed and direction are relative to the ship.

There was also a camera onboard the AA to monitor the sea state. Although the location of the camera was shifted several times during MARCUS, this camera still provides movie from which the sea state (i.e. open water, scattered ice or sea ice) can be identified. The sea ice were manually identified from the video data, and are shown in the Fig. 2.1 by pink and orange color near the Antarctic coast.

Weather balloons with radiosondes were launched at approximately 0000 Z, 0600 Z, 1200 Z, 1800 Z UTC each day during MARCUS to provide boundary layer thermodynamic profiles. For some times, the balloon-based data are not available as technicians could not access the ship deck in hazardous weather condition. The winds at the lowest levels were used to compare against those derived from the WXT 520 after correcting for ship motion.

2.3 Data cleaning and Quality Control

2.3.1 Customized application of ARM QC

The Australian "Atmospheric Baseline" program at Cape Grim in the SO region has included a long-term aerosol condensation nucleus observation. Gras (1995) previously found the climatological CN concentration during summer time over thee SO is 89.5 cm^{-3}.

However, in Figure 2.2 where red color illustrate the general total aerosol number condensation (CN) from the CPC, it can be noticed that there are both frequent and intense spikes happened during the MARCUS where the CN concentrations are orders of magnitude larger than previous observations made at close location. Further more, 71% of CN larger than 2000 cm^{-3} has a CO mixing ratio higher than 0.08 ppmv (figure not shown). It is therefore suspected that the spikes in CN are caused by the ship stack exhaust coming from the chimney on board.

Power generation in the ship stack burns hydrocarbon fuels and emits a range of combustion products including CO_2, water vapor, nitrogen oxides (NO_x), sulfur dioxide (SO_2), carbon moNO_xide (CO) and particulate matter including black carbon (BC) (Turner et al. 2017; Assessment 2009) etc. This means that the measurements of gases and aerosols from the AMF2 AOS represent a mix of background atmospheric aerosols and the emissions from the stack. All the aerosol instruments in Table **??** are affected at some times by ship stack contamination. Therefore it is necessary to remove the ship stack contamination from the natural background aerosol first to enable the scientific discussion about CCN-active aerosols over the SO.

Eliminating time periods with ship-stack contamination and to avoid eliminating periods where the aerosol probes were measuring background aerosols is challenging, because peaks in CN can also be associated with natural effects such as the presence of plankton blooms. Therefore, an algorithm described in Section 2.3.2 was developed to eliminate ship stack contaminated periods.

Data Quality Reports (DQR) issued by the ARM Data Quality Office were used as a first check of data quality to ensure the instruments were operating normally and representative of ambient conditions. Examples of eliminated data included those acquired during calibration mode of the CO analyzer, or during time periods when there was an unstable or blocked aerosol inflow in the UHSAS inlet. Each geo-physical variable measured by an

instrument has its own Quality Control (QC) report as a function of time given by a binary number. Each potential instrumental problem is represented as a binary digit.

Other quality flags determine whether the recorded data occurred within expected ranges or not. For example, based on the DQR QC flags set up for CPC, if the total concentration measured by the CPC was greater than $10^4 cm^{-3}$, the time period would be flagged as potentially invalid data. Similarly, if the CO mixing ratio from the CO-ANALYZERs is negative, another binary digit in the DQR QC will reflect measurement made at that time potentially be invalid data.

These above two kinds of DQR QC are treated differently for a customized QC on MARCUS data before the application of ship stack identification in the following section. For example, time periods with CO exceeding 0.08 ppmv were not automatically eliminated when the DQR QC flag indicated no other quality issues since it can provide useful information about ship stack.

2.3.2 Machine learning algorithm

According to the MARCUS observations, time periods with extremely large CO concentration typically coincide with times when there are spikes in CN concentration. Further, ozone concentrations decrease drastically at the same time when CO concentrations sharply increase. These two simultaneous signals caused by diesel insufficient combustion and NO_x titration near the stack outlet can be seen as a sign of ship-stack exhaust influenced pattern. For example, Fig 2.3 shows a zoomed-in view of part of the training data on 14th November, 2017. The red color represents manually identified ship stack. The above two figures plot scaled CO and O_3 concentration as training data, together with the bottom figure which plots CN concentration for comparison. The presence of the ship exhaust is seen through the sudden change of concentrations for CN, CO and O_3 at about 01:40 a. m. UTC. At that time, the CN has reached values hundreds of time larger its mean value of 239-492 cm^{-3} over the SO seen by Alroe et al. (2020)). The degree of ship stack contamination decreases

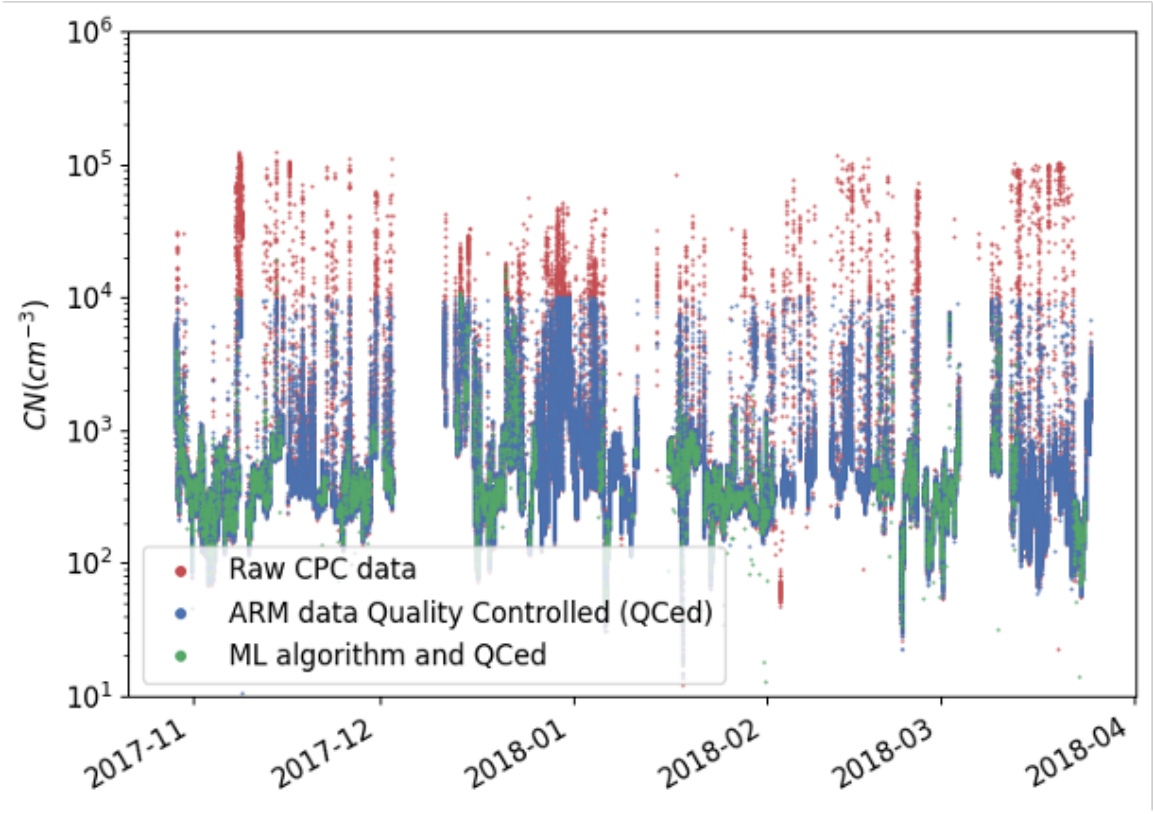

Figure 2.2: Concentration of aerosols with D >10 nm measured by the CPC, quality controlled by ARM QC flag only in blue and ARM QC flag combined with the Machine Learning derived ship stack flag in green through the whole MARCUS.

with time until 02:22 a.m. UTC, at which time all variables approach values similar to those before the ship exhaust encountered.

A Machine Learning (ML) algorithm was developed to train a Random Forest model to identify this pattern of CO increases and O_3 decreases to identify periods of ship exhaust. Considering their different variability, for example, the standard deviation of CO is one order larger than that of O_3, a normalized scale is defined to ascribe comparable weights to O_3 and CO concentration. The normalization used a standard scalar from the sklearn processing tool box (Pedregosa et al. 2011).

The training data used 13 No, 2017 and 14 Nov, 2017 CO and O_3 mixing ratio (in total 105125 samples) after customized application of DQR QC as mentioned in the Section 2.3.1. and after using sklearn standard scalar. The ship stacks in training dataset are manually labeled according to the size distribution from UHSAS and the ship motion parameters.

The missing CO and O_3 data are interpolated, then a rolling window of 300-second are used as pre-processing. Data acquired on 15 Nov, 2017 are used for validation. After sensitivity tests, for 15 Nov, 2017 data, 75% of time period identified as ship stack contamination by the model show corresponding high concentration from both CPC and UHSAS, and more importantly, much higher number concentrations for aerosols with D = 50 nm than the other aerosols with D $<$250 nm according to the HTDMA (figure not shown). It shows the production of higher small particles which can be a result of ship stack contamination. Thus, hyper-parameters were set up using 5 as the max depth of branches, 25 as total number of tree and 5 as the min number of leaves in model.

The fuel grade and engine power largely affect the products and processes of combustion through the chemical reactions happening near the chimney when the exhaust blends with local air masses over the monkey deck (Sinha et al. 2003). Due to insufficient combustion, the CO mixing ratio in the ship stack is substantially higher compared to that in the surrounding background atmosphere. The chimney also serves as a local point source

of nitrogen oxides (NO_x). Thus, for the locations in the immediate vicinity of the chimney, such as the inlet of AOS, O_3 concentrations are depressed through the process of NO_x titration (mainly by NO). This consists of the removal of O_3 through the reaction below. This NO_x titration has also been successfully captured and simulated in previous study by laboratory experiments and climate model (Tang et al. 2021; Hu et al. 2019).

$$NO + O_3 -> NO_2 + O_2$$

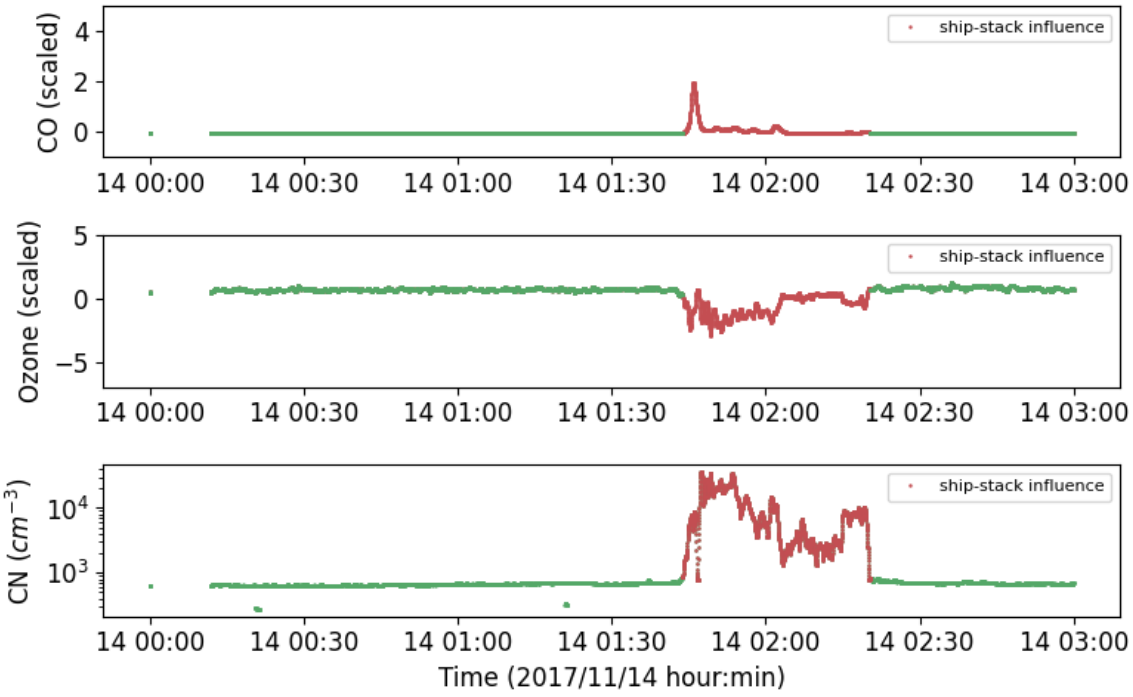

Figure 2.3: A Zoomed-in example of Machine Learning algorithm training data (scaled) on 14 Nov, 2017. It shows that the times (marked by red color) when CO concentration increases in the top figure, the O_3 decreases, as shown in the middle figure. This corresponds well with the spikes in CN concentration in the bottom figure. The green color stands for the time with values close to their the mean values.

Fig 2.3 shows part of the training data. Application of it can be seen from the figure **??** where spikes in CN concentrations and trace gas mixing ratio drastic changes indicate

the ship stack, they are also confirmed by aerosol size distribution from the UHSAS in the middle plot. Details about the setting up can be seen in the following section.

2.3.3 Setting up of contamination flag

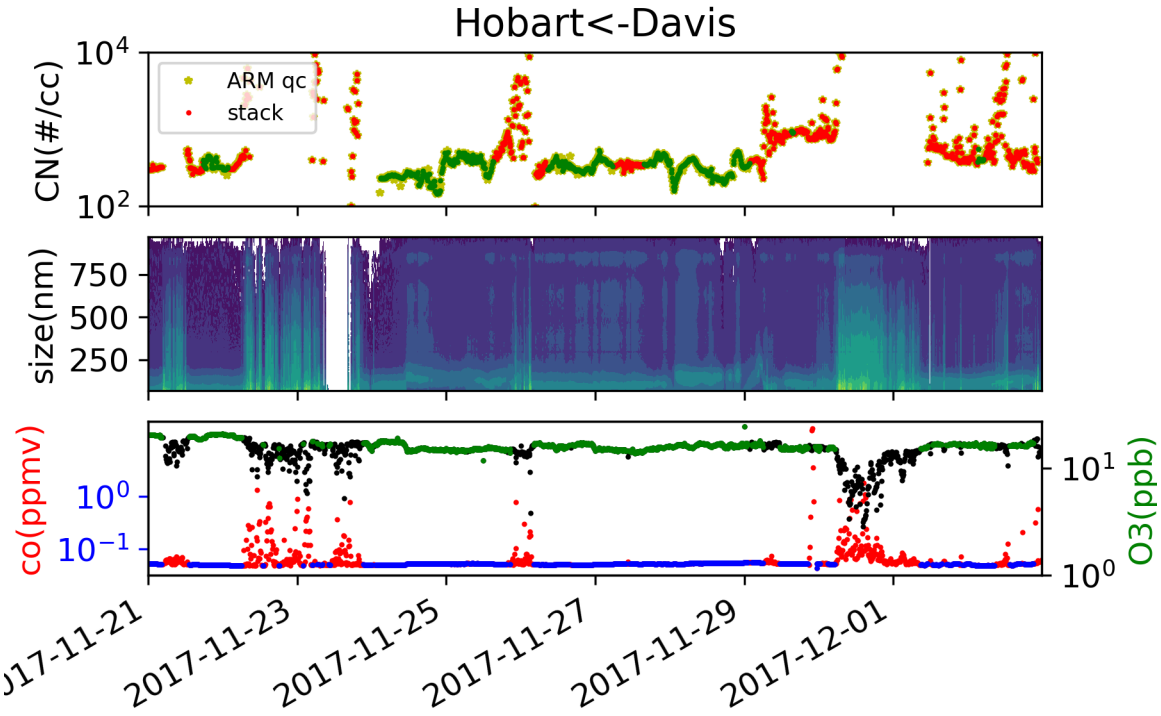

Figure 2.4: Trace-gases-derived ship contamination flag applied on CPC (top figure) and UHSAS (middle figure). In the top figure, the red color represents the stack identified used ML flag and DQR QC flag, the green color represent the values identified as ship-stack clean. The middle figure shows the size distribution where high concentration has color of yellow or light green. The bottom figure combined the CO and O_3 concentration curves together, with green and blue represent the ship-stack free O_3 and CO concentration respectively, and the black and red represent the ship-stack influenced O_3 in ppb and CO in ppmv.

The contamination flag derived from the above machine learning algorithm has been applied to data collected by all instruments listed in Table **??**. Figure 2.4 shows the application of the machine learning algorithm to data collected during the first voyage from Davis to Hobart. And its application on UHSAS for size distribution and CPC for CN. In general, the machine learning algorithm identifies 52% of the data from this voyage.

For comparison, the method in Humphries et al. (2021) identified 89% MARCUS data as contamination, suggesting its conclusions are more based on CAPRICORN II data with only 14% data identified as ship stack. Both the machine learning method and the method in Humphries et al. (2021) do not use the wind direction relative to ship motion to identify flow towards the AOS and potential contamination because the eddies that form around the ship's structure complicate the flow. Differences between these two algorithms also include that machine learning algorithm is applied by each voyage considering the V4 is different from the others, while the statistical method used in Humphries et al. (2021) treated MARCUS as a whole. Further, the machine learning algorithm developed here uses input of trace gases CO and O_3 while the Humphries et al. (2021) used CO and CN concentration as input. Avoiding the use of aerosol concentration as input to identify time periods of exhaust avoids the over-fitting the data and better potential of identifying time periods of enhanced aerosol concentration due to natural variability.

We compare the number concentration of CCN and accumulation mode aerosols measured from the UHSAS in Figure 2.5. This another between-instrument comparison after the customized QC shows the high efficiency for accumulation mode aerosol measured by the UHSAS to transfer into CCN and therefore confirmed its CCN-active characteristic.

2.3.4 Wind correction

Measurement of wind speed and direction by AOSmet are oriented to the ship bow instead of the true north. We correct these relative wind speed and direction with the method from

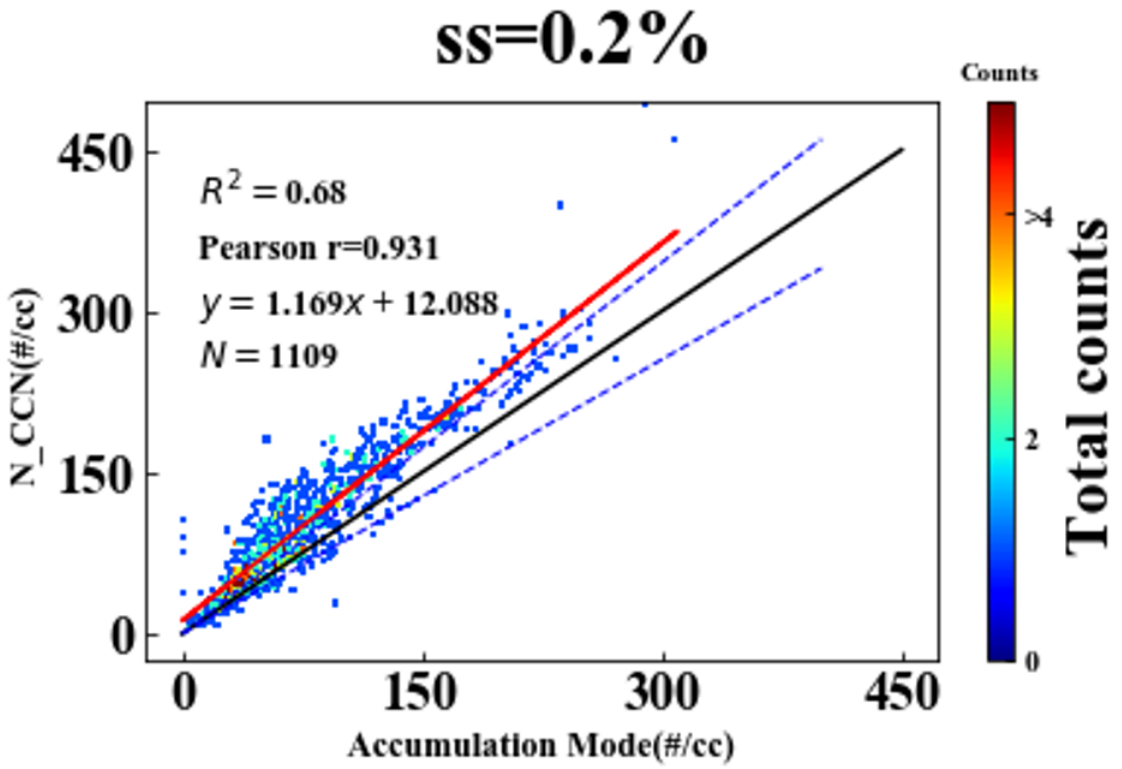

Figure 2.5: Correlation between accumulation mode aerosol and CCN measured at supersaturation 0.2%. Red line is the regression, black diagonal has a slope of one.

NOAA Technical Memorandum OAR PSD-311 and compare them to the wind measurement at the levels below 35 meters from the radiosonde.

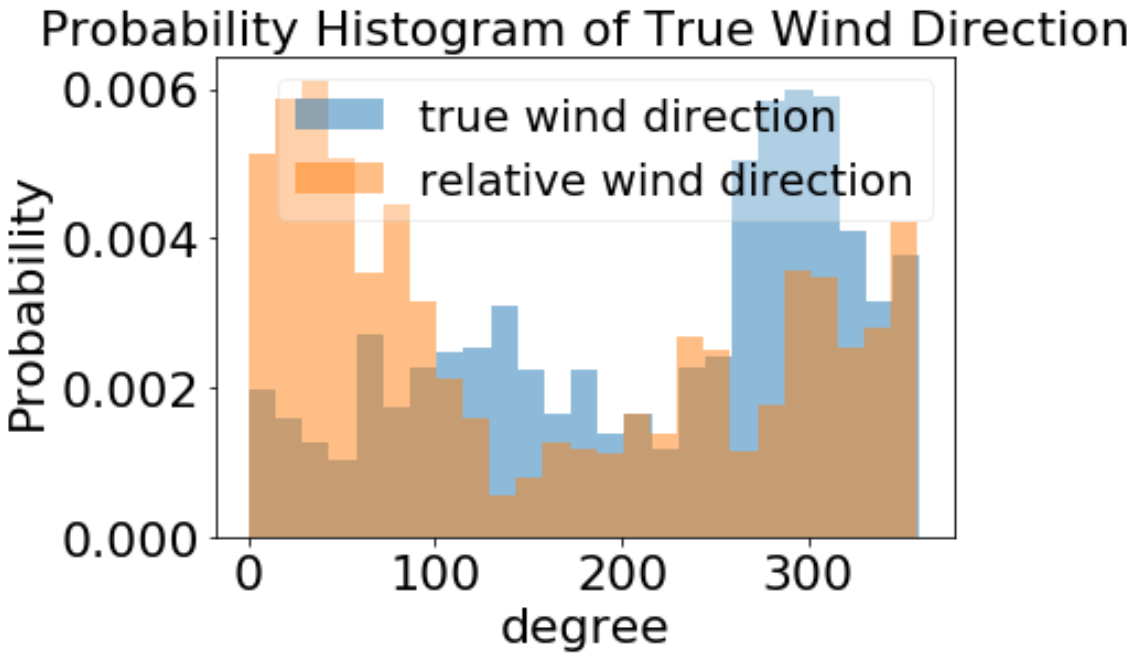

Figure 2.6: Normalized Wind direction histogram before (in yellow shade) and after (in blue shade) the wind direction correction

Figure 2.6 and 2.7 are normalized histograms to compare the wind distribution before and after the wind correction. The correction captures the dominate western wind with around 10 $m\,s^{-1}$. More detailed discussion about wind direction and speed can be found in Section 4.1.

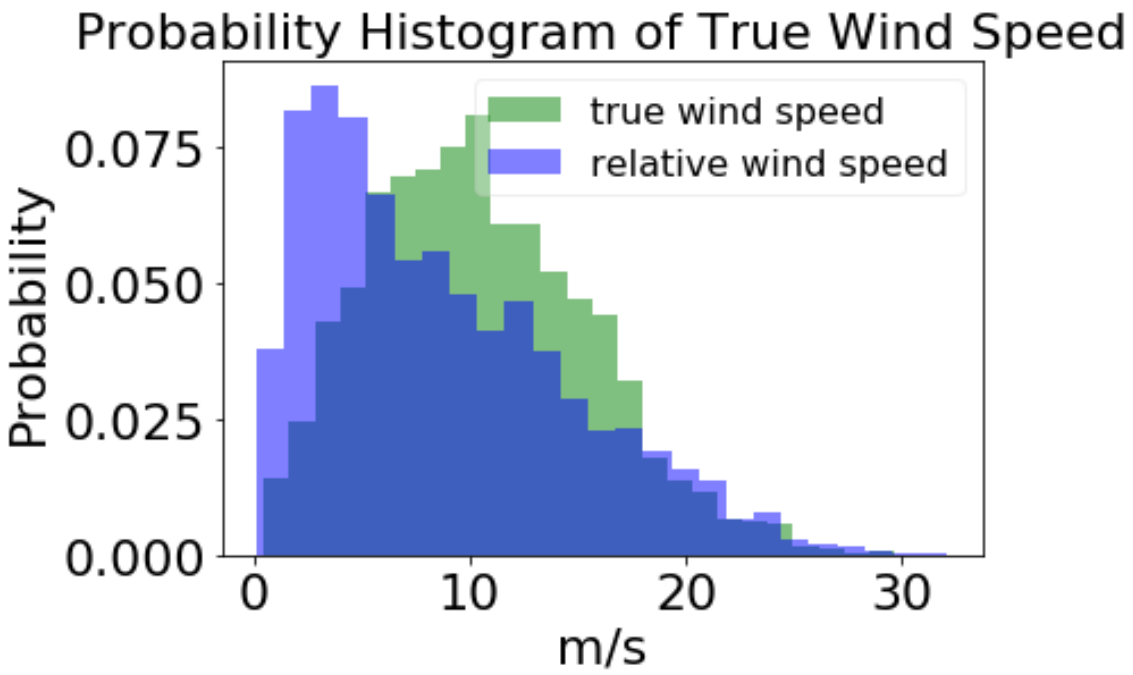

Figure 2.7: Wind speed correction, the normalized histogram of wind speed distribution before (in blue shade) and after (in green shade) the wind correction.

Chapter 3

Latitudinal Dependence of Aerosol and CCN properties

In this chapter the latitude dependence of the CCN-active aerosols and CCN properties over the SO are discussed, examining number concentration as a function of latitude (section 3.1) and physical properties such as the particle size distribution (section 3.2), hygroscopicity properties as Growth Factor (GF) (section 3.3), and optical properties such as scattering Angstrom Exponent (AE) and aerosol total scatter coefficient (Bs) at different wavelengths (section 3.4). Except when stated explicitly otherwise, statistically significant differences correspond to a confidence level of 0.05.

3.1 Number Concentration with latitude dependence

Recent aircraft-based cloud droplet number and below cloud CCN measurements over the Australasia SO imply an effective supersaturation of about 0.3% (Sanchez et al. 2021; Twohy et al. 2021). Therefore both supersaturation 0.2% and 0.5% are utilized in this MARCUS data analysis.

Figure 3.1 shows the latitudinal distribution of CCN concentration (N_{CCN}) over the SO at 0.2% and 0.5% supersaturation using data from all voyages during MARCUS after the removal of observations contaminated by ship stack. Error bars represent the variability with the bar extending between the first and third quartile for each one degree latitude bin. The mean CCN is represented as the solid circle and a line joins the median value of each bin. As latitude decreases from near Hobart (43°S) to near the Antarctic coast (67°S), both N_{CCN} at 0.2% supersaturation ($N_{CCN,0.2}$) and at 0.5% supersaturation ($N_{CCN,0.5}$) share the same trend, with their median values stay high north of 50°S, low between 50°S and 60°S and then increase south of 60°S.

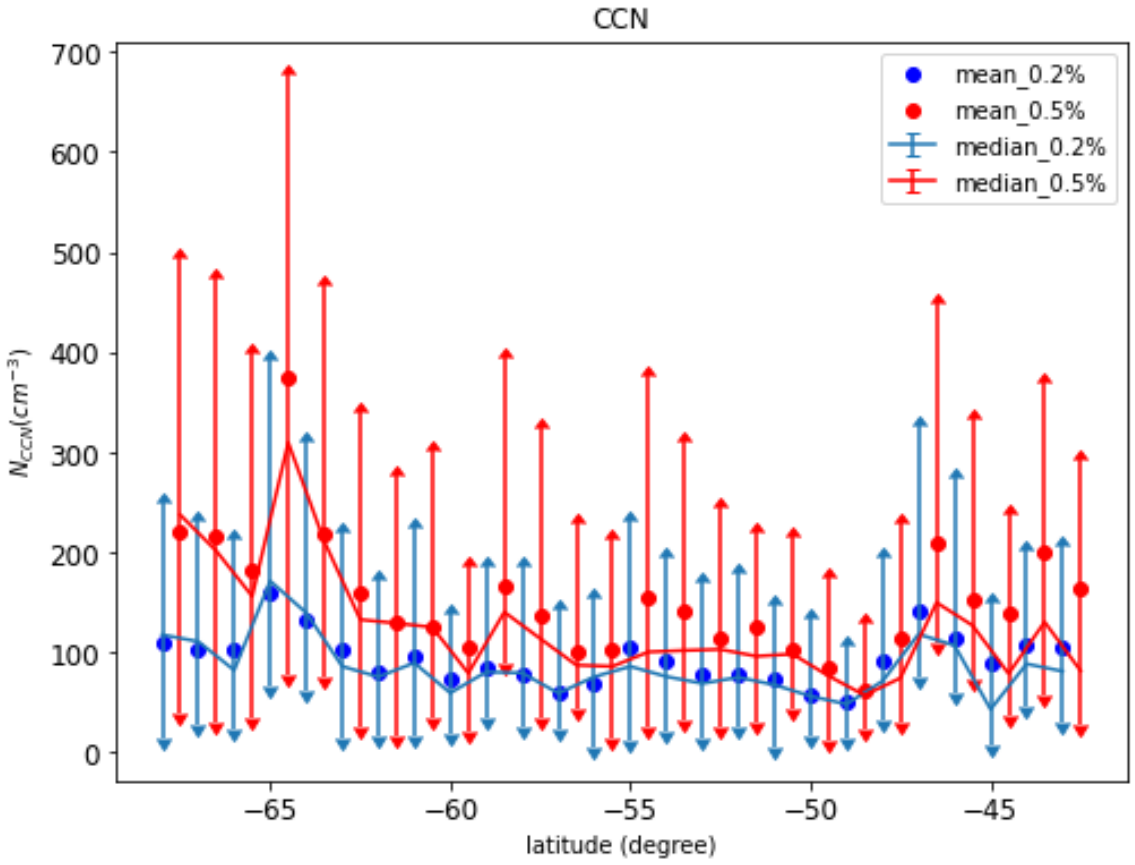

Figure 3.1: CCN concentration at 0.2% supersaturation (blue) and 0.5% supersaturation (red) latitudinal dependence. Lines connect the median concentration in each bin (one degree), round symbol stand for mean value, error bar with up limit for first quartile and down limit for third quartile

In detail, both $N_{CCN,0.2}$ and $N_{CCN,0.5}$ stay high between 43°S and 47°S with mean of 100 cm^{-3} and 117 cm^{-3}, then decrease to a minimum of 57 cm^{-3} and 63 cm^{-3} around 49°S. Between 50°S and 60°S, there is a smaller variation of $N_{CCN,0.2}$ ($N_{CCN,0.5}$) of 59-86 cm^{-3} and mean of 71.4 cm^{-3} (79-140 cm^{-3} and mean of 98.5 cm^{-3}), with a local minimum around 57°S. South of 60°S, the $N_{CCN,0.2}$ ($N_{CCN,0.5}$) generally increases from 60 cm^{-3} (79 cm^{-3}) to 118 cm^{-3} (238 cm^{-3}) near the Antarctic coast, with a local maximum 171 cm^{-3} (310 cm^{-3}) around 65°S.

	Latitude Bin (°S)	Mean (cm^{-3})	Median (cm^{-3})	Count	Std. Dev	Min (cm^{-3})	Max (cm^{-3})	25th Percentile	75th Percentile	Independent sample number
$CCN_{0.2}$	60-68	110	109	488	52	7	331	71	138	93
	50-60	83	76	366	40	9	211	55	103	81
$CCN_{0.5}$	60-68	206	199	473	133	10	1449	124	255	96
	50-60	131	101	367	89	13	627	70	161	80

Figure 3.2: Statistics for $N_{CCN,0.2}$ and $N_{CCN,0.5}$ for latitude range between 50°S and 60°S and south of 60°S using MARCUS data after ship stack removal.

Humphries et al. (2021) also analyzed the latitudinal dependence of $N_{CCN,0.2}$ and $N_{CCN,0.5}$ for a similar time period using both MARCUS and CAPRICORN2 data, but used a more restrictive ship stack identification scheme to remove contaminated data. It left only 11% of MARCUS data as ship-stack-free and combined with the left 86% of CAPRICORN data. Although the latitudinal variation illustrated in Humphries et al. (2021) was thus largely dominated by the CAPRICORN data (61% data are from CAPRICORN and 39% data from MARCUS), patterns should be comparable as all data were obtained in the Australasian sector of the SO during the same Australia summer.

According to the Hysplit4 back trajectories results in Humphries et al. (2021), continental and authropogenic sources from the coast of Tasmania, Australia add to the background marine atmosphere in the northern sector of around 45°S. To study background marine

aerosols and CCN and associated processes, the northern part of the SO (north of 50°S) is removed for the following analysis. For the SO between 50°S and 68°S, both results illustrate larger $N_{CCN,0.2}$ south of 62°S and lower $N_{CCN,0.2}$ between 50°S and 60°, with MAD result states mean of 125 cm^{-3} and 102 cm^{-3} and ML algorithm result shows mean of 110 cm^{-3} and 83 cm^{-3}. Table 3.2 is a statistical chart especially designed to be similar to the Table A1 in Humphries et al. (2021) for algorithm result comparison convenience if readers are interested. Both of them show significant different median and mean values between 50°S - 68°S and south of 60 °S. But the ML QC derived both $N_{CCN,0.2}$ and $N_{CCN,0.5}$ concentration are significant higher than those derived from Humphries et al. (2021).

As chart shown in Figure 3.2, $N_{CCN,0.5}$ are measured at higher supersaturation and are generally higher than $N_{CCN,0.2}$. Figure 3.1 also shows that the gap between $N_{CCN,0.2}$ and $N_{CCN,0.5}$ largely increase at south of 60°S, from a mean of 29 cm^{-3} between 50°S and 60°S to 79 cm^{-3} south of 60°S. Gras and Keywood (2017) studied the SO airborne particles measured near the Cape Grim ($40°39'S, 144°44'E$), noted typically $CCN_{0.5}$ (particles active at a supersaturation of 0.5%) includes particles with dry diameter larger than approximately 50 nm whereas $CCN_{0.23}$ (particles active at a supersaturation of 0.23%) includes particles with dry diameters larger than 78 nm. At given chemical composition, this implies a large number of particles with dry diameter between 50 and 78 nm become CCN if a 0.5% supersaturation threshold has been met. On the other hand, between 50°S and 60°S there does not appear to be as many aerosols in this size are being activated into cloud drops. This high increase of $N_{CCN,0.5}$ relative to $N_{CCN,0.2}$ might be caused by the change of aerosol size distribution, which will be discussed in section 3.2. However, the chemical composition between the two regions can also change, along with its physical properties such as hygroscopicity, which will be discussed in section 3.3. Quinn and Bates (2014) summarized the different sea salt to non-sea-salt sulphate (nss-sulphate) ratio as a function of geometric mass diameter at 70% using data acquired on cruises over the SO, finding the dominance of sea salt on the marine aerosol mass size distribution is only significant for aerosols with D

larger than about 600 nm between 40°S and 70°S. It also reveals the chemical composition and size distribution are coherently related with each other over the SO.

Considering the motivation of this study is to explore the sources and sinks of background aerosols and CCN in the pristine marine SO environment, the latitude range between 50°S and the Antarctic coast is focused upon to exclude a major influence of aerosols transported from Australia. The above N_{CCN} difference between two latitude ranges (between 50°S and 60°S and south of 60°S) inspires the examination of differences in size distribution and physical properties, and the insights that provides about sources, sinks and meteorological controls in the rest of this thesis.

3.2 Size Distribution

Figure 2.5 shows that there was a strong correlation (0.93) between the accumulation mode aerosol and CCN concentrations. Thus, examining how the properties of accumulation mode aerosols very with latitude might help to explain the CCN variability. Here, the accumulation mode aerosols are divided into different size ranges in an effort to understand processes that affect their distribution as a function of latitude.

Figure 3.3 shows that the aerosol concentration of aerosols with 100 nm <D <350 nm ($N_{100-350}$) generally increases as latitude decreases. South of 60°S generally has higher concentration median $N_{100-350}$ (69.3 cm^{-3}) than 50-60°S with a concentration of 42.5 cm^{-3}. In general, the $N_{100-350}$ range (minimum 22.2 cm^{-3} around 50S and maximum 88.0 cm^{-3} off Antarctic coast) is the closest to the $CCN_{0.2}$ range (minimum 56.4 cm^{-3} near the 50S and maximum 171.3 cm^{-3} near the 65S) compared to $CCN_{0.5}$, which shares the same general trend as well. This can be understood as the most aerosols between 100 and 350 nm in size are already activated at 0.2 SS. This will later be discussed following the discussion about particle number size distribution. The blue vertical line indicate a critical latitude, 60°S, since the patterns north and south of the 60°S have the largest differences.

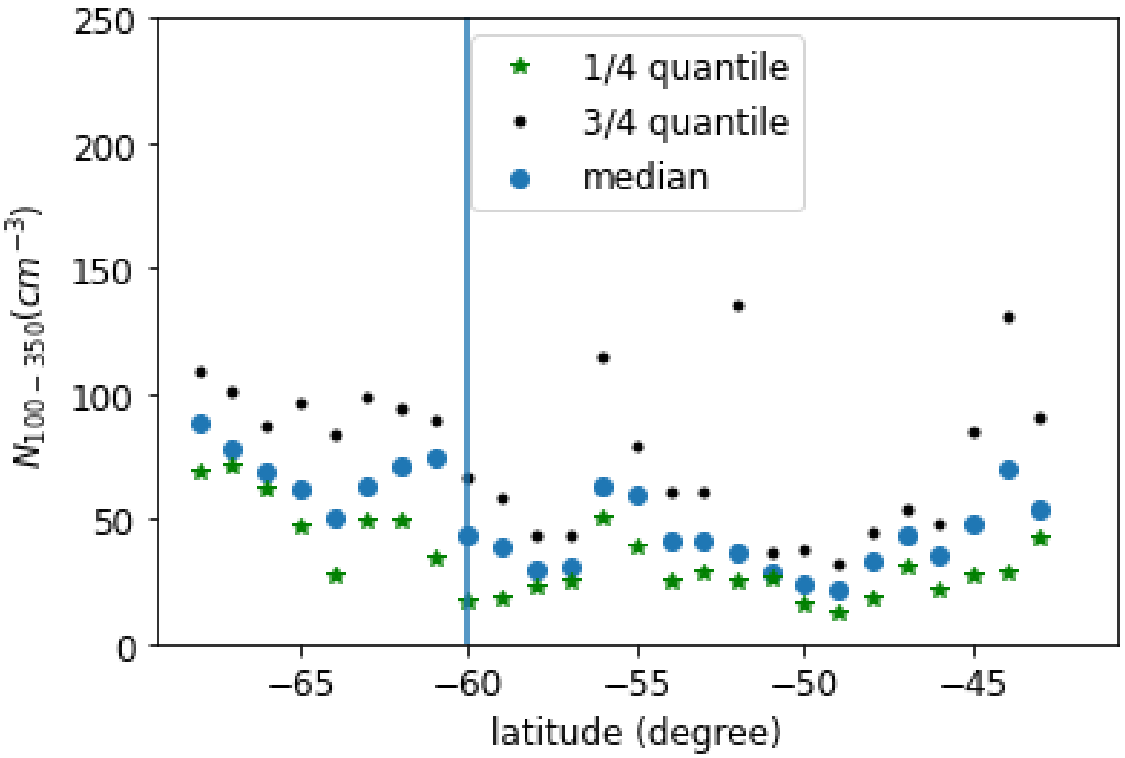

Figure 3.3: $N_{100-350}$ as a function of latitudes, with round symbol for median value, green star for the first quartile, black symbols for the third quartile at each one degree wide latitude

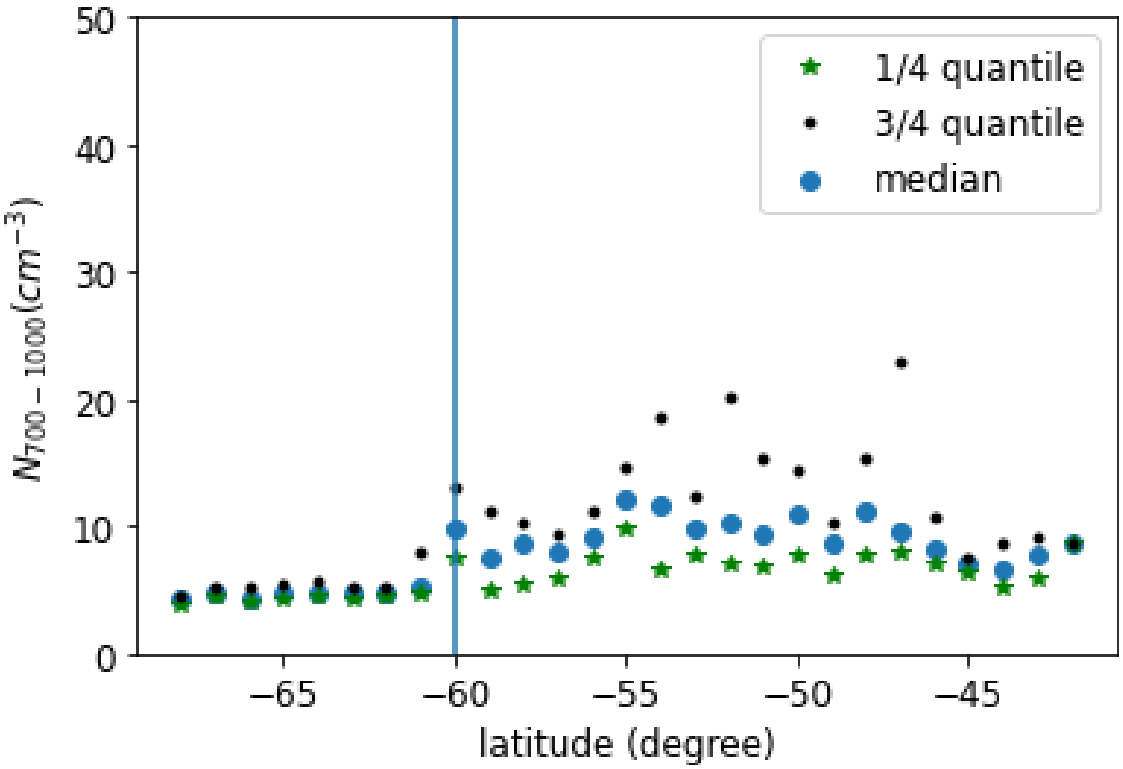

Figure 3.4: $N_{700-1000}$ as a function of latitude, with round scatter for median value, green star for the first quartile, black scatter for the third quartile at each latitude

This critical latitude, is also apparent in Figure 3.4, where the mean value of ($N_{700-1000}$) south of 60°S is 4.7 cm^{-3}, and gradually increases as latitude increases. The 50-60°S has 9.8 cm^{-3} as median $N_{700-1000}$ (increased more than 105%). The 50-60°S SO also has larger variability than south of 60°S, as illustrated by the large values of third quartile points (black point marker). While the first, third quartile together with the median value overlap with each other, suggesting very small variability for $N_{700-1000}$ south of 60°S.

This can be explained from two perspectives. First, particles with 700 nm <D <1000 nm range are large particles in the accumulation mode category, which may contain higher sea salt aerosol ratio. It has been well acknowledged that particles sizes greater than 1000 nm are almost exclusively composed of primary sea-salt aerosol in pristine marine boundary layer while new particles in nucleation mode are believed to comprise nss-sulphate and organics Quinn and Bates (2014). As such, the accumulation mode aerosols that can potentially become CCN encompasses all types of aerosols, but with different compositions in different size ranges or under various physical scenarios. From this perspective, the sea salt aerosol fraction can be higher in 50-60°S whilst less south of 60°S. This is confirmed in Humphries et al. (2021), corresponding to the higher chloride fractional aerosol composition between 50-60°S and the minimum of that in the southern-most 5 degree bin.

Another perspective which can support this besides the shift of chemical fractions that consist of particles with 700 nm <D <700 nm can be their surrounding environments. Comparing Figure 3.4 to Figure 3.3, a potential explanation for the different sign can be that the surrounding meteorological environment favor the production of sea-salt aerosol in 50-60°S, while favors the production of nss-sulphate and other secondary aerosols south of 60°S. Aerosol sources and sinks in these two latitude ranges is discussed in Chapter 4 to describe these observed trends.

Aerosol number distribution and surface area distribution with 70 nm <D <1000 nm range ($N_{70-1000}$) can be seen in Figure 3.5 and Figure 3.6, which gave us a broader view of accumulation mode aerosol distribution in 50-60°S and south of 60°S. It shows the

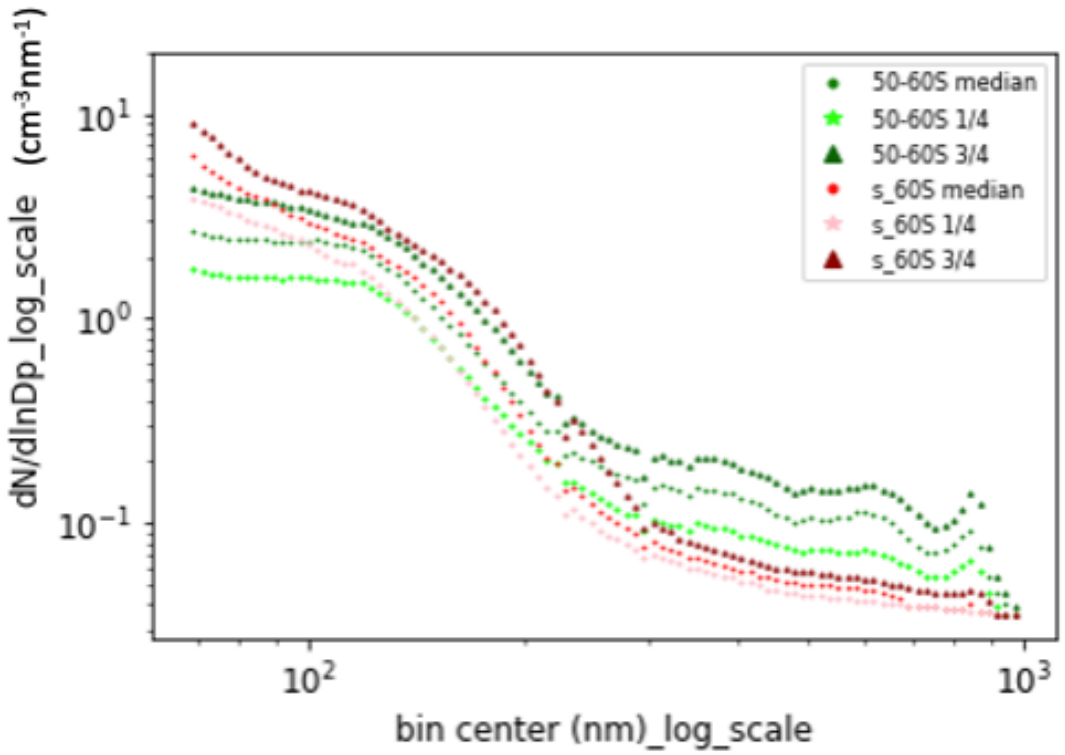

Figure 3.5: $N_{70-1000}$ number distribution measured by UHSAS in log scale, green representing 50-60°S while red representing south of 60°S, the colors from dark to light respective show the third quartile, median value and the first quartile.

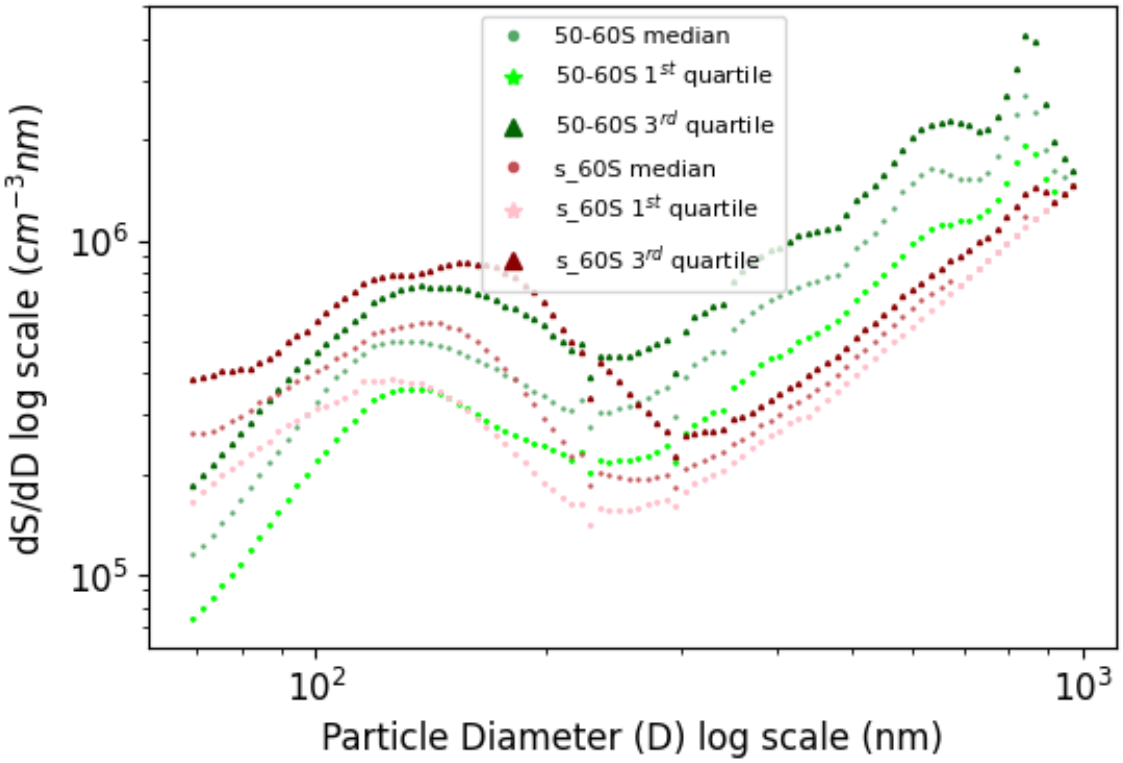

Figure 3.6: $N_{70-1000}$ surface area distribution derived with UHSAS data in log scale, green representing 50-60°S while red representing south of 60°S, the colors from dark to light respective show the third quartile, median value and the first quartile.

number concentration generally decreases with particle diameter. In other words, particles within 70 nm <D <300 nm dominate the number of accumulation mode aerosol. For particles within 70 nm <D <300 nm range, number concentration is higher south of 60°S while for particles larger than 200 nm, number concentration is higher in 50-60°S latitude range. Considering the figure is log scaled and the total number of aerosols measured by UHSAS is dominate by small particles, in general $N_{100-350}$ should be higher south of 60°S since it has more small particles, and this is consistent with the NCCN latitude dependence measurements above.

The curve shapes are different in Figure 3.6 because of the square of radius is used when calculating the surface area. It therefore reflects more information about the aerosols optical properties which we will discuss in more detail in the following section 3.4. Figure 3.6 reveals the dominant role played by particles larger than 300 nm, its closeness to the wavelengths used by particle soot absorption photometer (PSAP) implies the Rayleigh scattering is supposed to be the primary scheme for the bulk scattering properties used to derive scatter AE and single scattering albedo. It also notes a mode near 150 nm caused by highly concentrated small particles shown in Figure 3.5. The variability (expressed by the spread of the lines) measured near this mode is much higher compared with the other size range especially for measurement made south of 60°S. It partly reveals the large variability for particles with 70 nm <D <300 nm range near the Antarctic coast. This may be caused by the high variability of nss-sulphate, which has been studied as a function of seasonality and chlorophyll concentration near the sea-ice melting margin area. The frequent precipitation (figure not shown) along the storm track in 60-62°S latitude range during the MARCUS campaign may also contribute to the large variability. This can also be part of a measurement uncertainty due to a limited sample size south of . The ship's moving speed decreases as the sea ice increases up south of 60°S, leading to more ship stack contamination. Together with some removal of the data when the AA stays in the port, the remaining amount of "clean" aerosol south of 60°S after the removal of contamination results in high

measurement uncertainty which can also be seen in other measurements such as optical properties and hygrocopicity. This was carefully considered in this study to make sure the statistical variability is still of significance from observations south of 60°S. That being said, more observations in this area are strongly needed in future filed campaign, which we will discuss more in the Chapter 5.

3.3 Hygroscopicity

Hygroscopicity is a fundamental aerosol property and that describes the tendency of an aerosol to absorb water vapor from the environment in order to grow. A widely used parameter to quantify hygroscopicity is the aerosol particle size hygroscopic GF. It is defined here as the ratio of the wet particle diameter at a high Relative Humidity (RH) of 80% to the corresponding dry diameter. A higher GF means that an aerosol is more capable of absorbing water.

Figure 3.7 shows the normalized density distribution of different size aerosols' GF in two regions, north and south of 60°S. In the latitude range of 50-60°S, the GF increases as aerosol size increases, from the minim GF mode near 1.30 for 50 nm particle to its maximum mode near 1.67 for 250nm particles. This increase trend in 50-60°S means the larger the particles, the more capable they are to absorb water vapor from the environment. For the latitude range south of 60°S, the GF mode has a range of 1.34-1.41, being quite stable for different size of aerosols.

Asmi et al. (2010) measured the hygroscopicity of summertime sub-100 nm aerosol off the Antarctic coast at station Aboa using an impactor for the size-segregated composition of marine aerosol particles, pointing out that the measured hygroscopicity GF at 90% RH is 1.68 for 50 nm particles and 1.71 for 90 nm particles, while the hygroscopicity GF at 80% RH is 1.41 for 50 nm particles and 1.42 for 100 nm particles. Although the absolute values can not be compared under different RHs and the measurements are taken from different part of Antarctic, both of them have the air origin from the Antarctic according

to the Hysplit which will be discussed in the next section, and at least both keep their GF stable between 50 nm and 90 nm/100 nm aerosol. It also pointed out most of the sub-100 nm particle hygroscopicity can be well explained by a large fraction of non-neutralised sulphuric acid together with organic material, and the hygroscopicity variability was mainly driven by inorganic salts.

Although aerosol chemical composition information during the MARCUS will be extremely helpful, there are no aerosol mass spectrometers on board. Previous studies such as Xu et al. (2020) have used the common chemical composition for marine aerosols as comprising organic matter, non-sea-salt sulfate, nitrate, ammonium, sea salt and black carbon (BC) etc., applying various mixing rule to predict aerosol hygroscopicity. However, the reverse process would be much more challenging. From Figure 3.7, it infers the chemical composition of particles with 50 nm <D <250 nm range south of 60°S does not change a lot as particle size changes, and it is expected to be a result of high ratio of sulfur-based aerosol considering its low GF value range of 1.3-1.4. Between 50°S and 60°S, the GF strongly dependet on the wavelengths and therefore organic or BC is expected to contribute to the low value of GH for 50 nm particle.

3.4 Optical Properties

Angstrom et al.(1929) noted the spectral dependence of extinction by particles may be approximated as a power law relationship (Eq 3.1), where λ is the wavelength in microns of the corresponding aerosol optical depth (AOD) values, α is unitless AE and β is Angstrom's turbidity coefficient which equals AOD at $\lambda = 1\ \mu m$. Thus, AE is a qualitative indicator of wavelength dependence of AOD to obtain basic information on the aerosol size distribution aerosol particle size and the spectral curvature of the Angstrom exponent contains useful information about the aerosol size distribution.

$$AOD(\lambda) = \beta \times \lambda^{-\alpha} \tag{3.1}$$

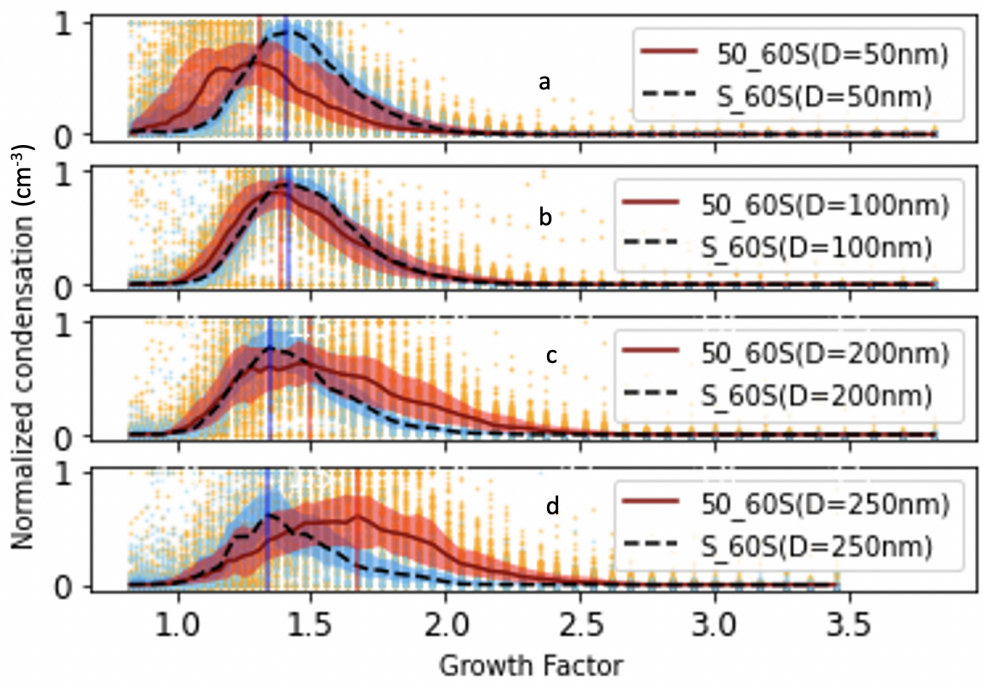

Figure 3.7: Hygroscopic Growth Factor normalized density distribution for particle sizes (50, 100, 200, 250 nm from a to d) from the HTDMA, red color and blue color represent the latitude range between 50 and 60°S and latitude range south of the 60°S, the lines plot their median values with shading corresponding to the first and third quartile value. The red line is the mode for GF south of 60°S and the blue line for GF mode between 50-60°S

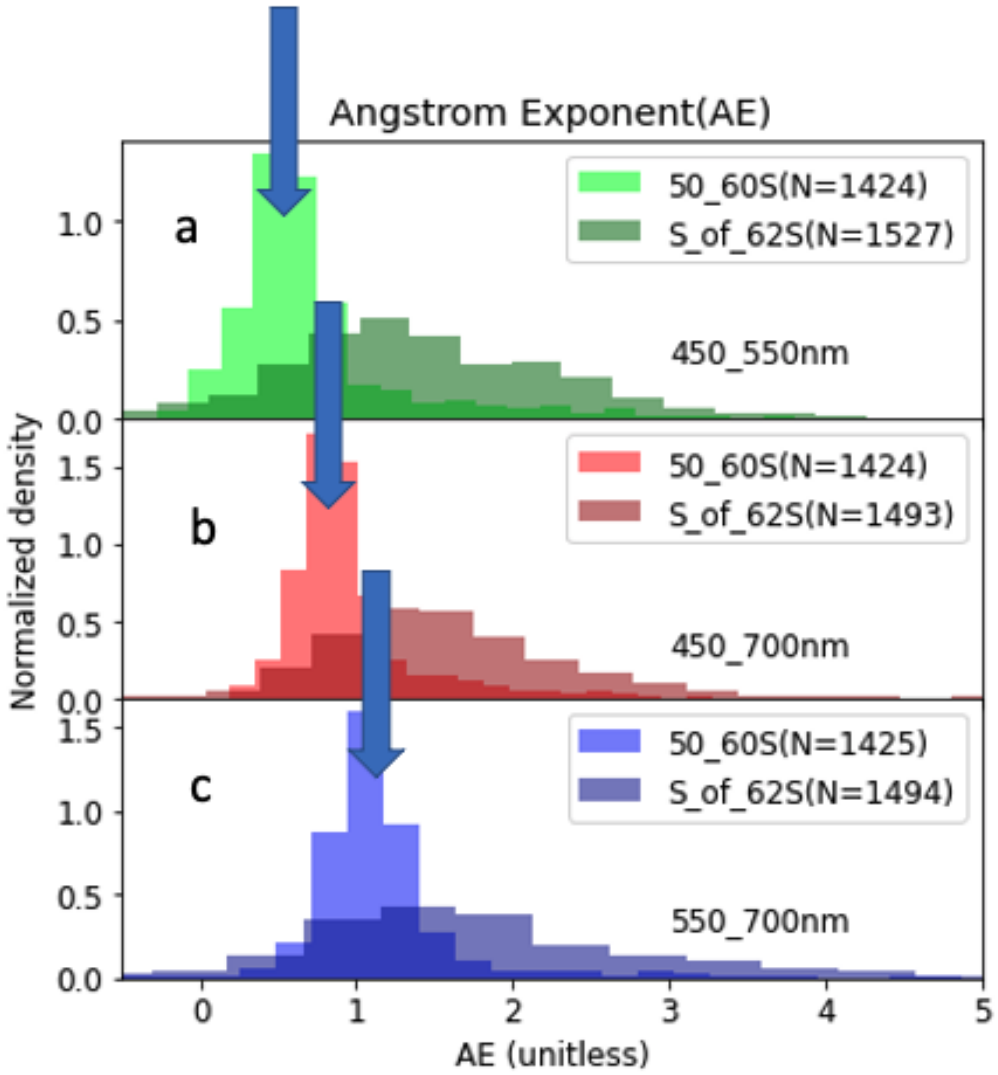

Figure 3.8: Sub-micron SO aerosol Angstrom Exponent (AE) normalized density distribution from nephelometer in the latitude range between 50 and 60°S and latitude range south of the 60°S. From the a to c are the AE derived with different pair of wavelengths, as shown in each figure by text under the legend. The arrows show the increase of AE mode as wavelength increases.

This model is intensively used in satellite-borne aerosol remote sensing where AOD are acquired by vertically integrate the blocking of sunlight by absorbing or by scattering light, as an indicator of the aerosol loading in the entire vertical column of the atmosphere. For this study using ship-borne nephelometer and PSAP, instead, we separately measure the scatter and absorption properties to derive the scattering AE and absorption AE to analyze the aerosol properties in the measured sample near the surface. The scattering AE reflects more information about aerosol size while absorbing AE reflects more about aerosol type and chemical composition.

Taken the ratio of Eq 3.1 at two different wavelengths and then taking the logarithm the Angstrom wavelength exponent can be computed from spectral values of Bs by (the subscript number 1 and 2 stand for discrete wavelength):

$$\alpha = -\frac{dlnBs}{dln\lambda} = -\frac{ln(Bs_2/Bs_1)}{ln(\lambda_2/\lambda_1)}. \tag{3.2}$$

According to the 3.1, spectral variability of Bs therefore contains information about the aerosol size distribution and a basic estimation of the prevalent radius of the observed aerosol. For the two extreme ends of AE range, if AE is close to 4, it represents Rayleigh scattering on particles that are small compared to the wavelength of visible light, and if AE close to zero or even slightly negative values, it represents geometrical optics and large particles which normally appearing in clouds for example is true of cloud particles (with typical sizes $>5\ \mu m$).

Figure 3.8 shows the normalized density distribution of scattering AE between 50°S and 60°S (light color) and south of 62°S (dark color) for aerosol only smaller than 1000 nm. The dark color has higher AE modes for all the pairs of wavelengths, mode of 1.1 for alpha measured with 450 nm and 550 nm wavelength ($\alpha_{450-550nm}$), 1.4 for alpha measured with 450 nm and 700 nm wavelength ($\alpha_{450-700}$) and 1.5 for alpha measured with 550 nm and 700 nm wavelength ($\alpha_{550-700}$). While the light color with lower AE modes between 50°S and 60°S, 0.5 for $\alpha_{450-550nm}$, 0.8 for $\alpha_{450-700}$ and 1.0 for $\alpha_{550-700}$. In general, AE

in both latitude range is smaller compared to the similar latitude at Northern Hemisphere (Posyniak and Markowicz 2009), which is potentially due to sedimentation of large particle in the course of long range transportation of pollution south of 50°S. While to compare between these two latitude ranges, the differences of AE (significant at 0.05 level) show atmospheric aerosol acquired south of 62°S consists of relatively small particles and that between 50°S and 60°S consists of relatively large particles. This is consistent with the aerosol size distribution in Figure 3.5 and 3.6 with similar potential reasons we previously talked.

There is also a similarity between the regions as both of their AE increase as the average wavelength increase though with different magnitudes. A more precise empirical formulation between AOD and wavelength can be retrieved from the second order polynomial fit equation in Eq 3.3 instead of a linear fit as Eq 3.1:

$$lnBs(\lambda) = \alpha_0 + \alpha_1 ln\lambda + \alpha_2 (ln\lambda)^2, \tag{3.3}$$

$$\alpha'(\lambda_i) = \frac{d\alpha}{dln\lambda} = -2\alpha_2. \tag{3.4}$$

The derived α' according to the Eq 3.4 is 2.24 for latitude between 50°S and 60°S and 1.80 south of 62°S. Both of them are positive value, implying the second order polynomial become a negative curvature (convex), which specify a dominance of fine mode aerosol particles. Therefore, the AE confirms the fine mode (particle diameter smaller than 200 nm) aerosol are the dominant mode in both area, while the effective radius south of 62°S is smaller than aerosol between 50°S and 60°S.

Chapter 4

Meteorological controls of aerosols over the SO

In this chapter, the meteorological controls of concentrations of the accumulation mode aerosols and CCN between 50°S and 60°S and south of 60°S are explored in order to identify as their potential sources and sinks.

4.1 Horizontal wind

As mentioned in the Chapter 1, both primary marine aerosols as SSA and secondary aerosols originating from gas to particle conversion near the surface with precursors coming from the ocean are believed to be controlled by the horizontal wind speed. In this section, the dependence of aerosols on wind speed is examined separately for the latitude range etween 50°S and 60°S and south of 62°S. The latitude range 60 and 62°S serves as a transition between the Polar Cell near the Antarctic and the Ferrell Cell between 30°S and 60°S (Ferrel 1859; Simmons et al. 2021). This shifting of large scale atmospheric circulation between these two regions affects the air mass movement as well as the properties of aerosol in these regions.

Figure 4.1 shows the frequency of horizontal wind speed and direction between 50°S and 60°S measured by the AOSmet system, corrected with ship motion parameters and confirms with the radiosonde-borne wind direction at its lowest two levels when the balloon is less then 35 meter above the sea surface. Details can be found in Chapter 2. Figure 4.1 illustrates the wind direction as rose plot. Wind in this latitude range primarily comes from between W and WNW (85% of the time), with only seldom wind from N, WSW and SW. There are no wind from E. Thus, the large portion of green color implies the highest frequency of wind speed between 10 $m\ s^{-1}$ and 15 $m\ s^{-1}$. The largest wind speed (above 20 $m\ s^{-1}$, colored in dark brown) shows up mainly from the WNW, sometimes from the

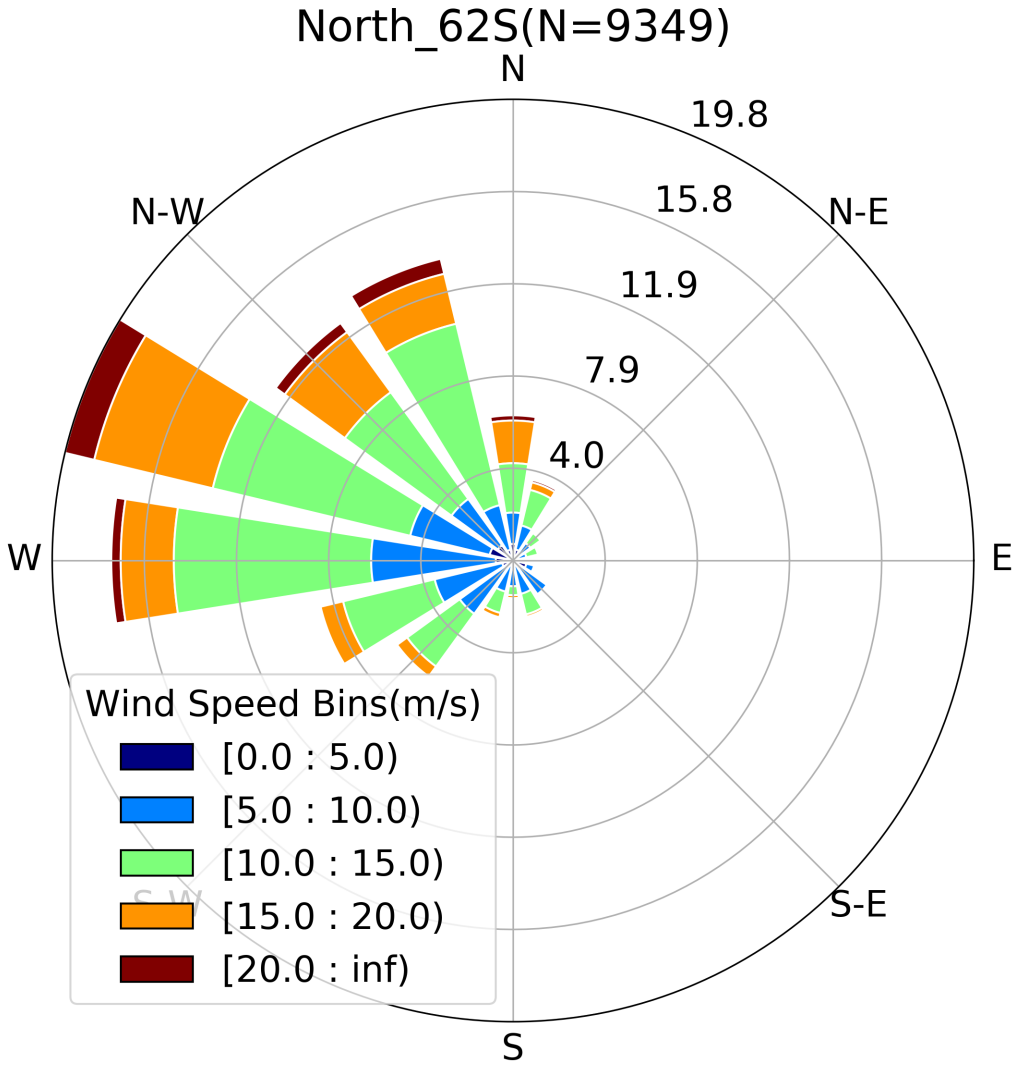

Figure 4.1: Horizontal wind distribution north of 62S, with radius representing the wind speed in meter per second and area of different colors standing for the frequency in that specific direction for the whole MARCUS, wind speed bin size are noted in legend.

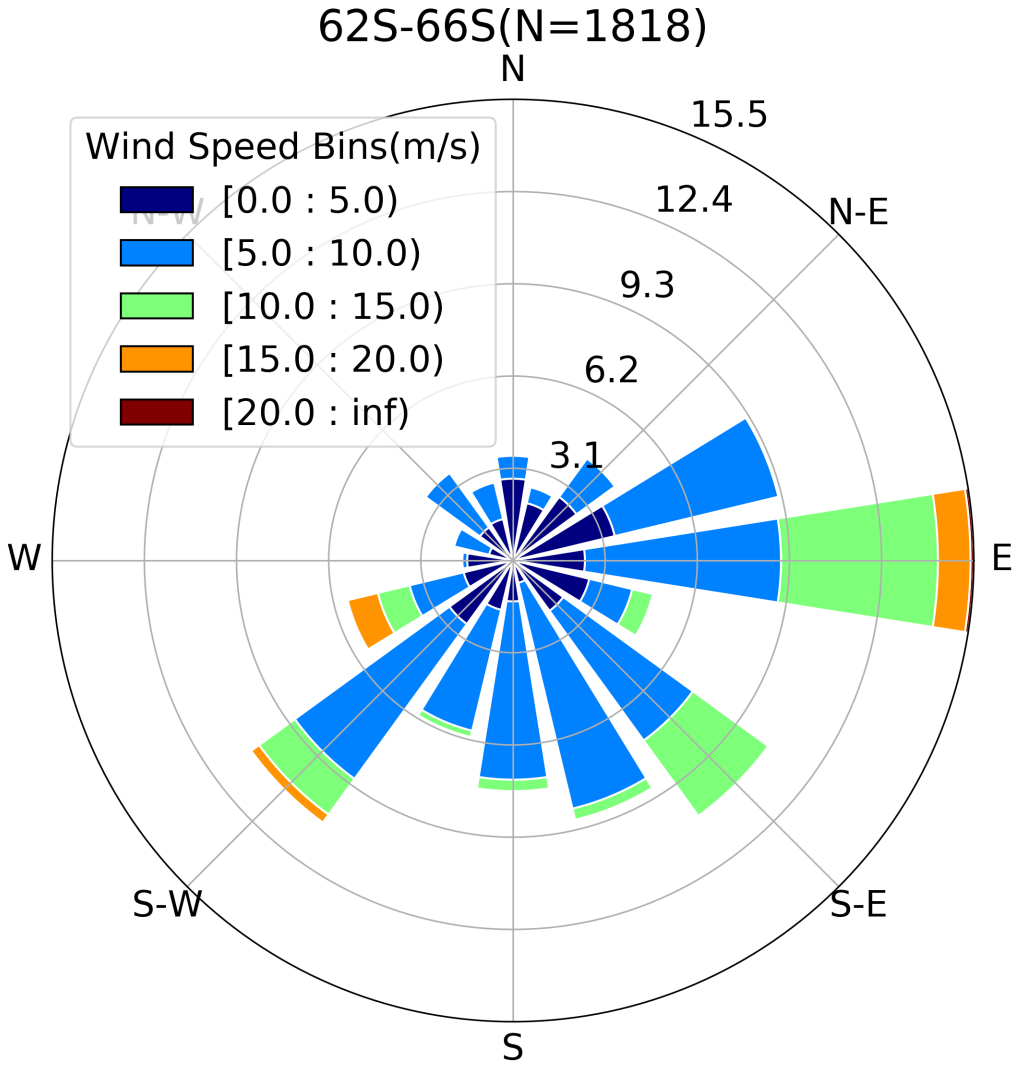

Figure 4.2: Horizontal wind distribution south of 62S, with radius representing the wind speed in meter per second and area of different colors standing for the frequency in that specific direction for the whole MARCUS, wind speed bin size are noted in legend.

W, NNW and N. These strong wind events are a notable feature of the Antarctic climate system and have been observed by other studies in this region (Gras and Keywood 2017; Derkani et al. 2021). 37% of the time the observed wind between 50°S and 60°S is larger than 15 $m\ s^{-1}$. The corresponding wind directions are consistent with expectations from the Ferrell Cell, where lower tropospheric westerlies converge over the SO because of the limited land and topography compared to the northern hemisphere offers less impediment to the flow (Ferrel 1859).

Figure 4.2 shows the frequency of horizontal wind speed and direction south of 62°S in a similar way. There is no brown color seen on the in Figure 4.2, implying no wind with speed larger than 20 $m\ s^{-1}$. There are only 12% of winds have speed larger than 15 $m\ s^{-1}$, and they are dominantly come from E, WSW and SW. Most of the colors are seen in the bottom half of the circle, shows overall 76% of winds have a southerly component. The blue color which stands for the wind speeds between 5 $m\ s^{-1}$ and 10$m\ s^{-1}$ were most frequent, occurring 71% of the time. In the Polar Cell, cold air descends from the Antarctic plateau as a large-scale synoptic forcing, which together with the local katabatic wind effect and the land topography, results in the frequent southerly wind (Mather and Miller 1966).

In summary, the winds measured during MARCUS show that between 50°S and 60°S there are larger wind speeds predominantly from the west, while south of 62°S the wind speeds are more southerly.

Examining the correlation between wind speed and N_{CCN} and aerosols can provide insight into aerosol sources in the two different regions. Figure 4.3 shows the relationship between $N_{CCN,0.2}$ and horizontal wind speed on the left, with a slope of 0.016 ($s \cdot m^{-1} cm^{-3}$), and P value less than 0.01 (less than 0.01 probability that the correlation between wind and $N_{CCN,0.2}$ in the sample data occurred by chance). This positive correlation shows $N_{CCN,0.2}$ increases with wind speed for measurements made between 50°S and 60°S. On the other hand, Figure 4.3 shows a smaller positive correlation between $N_{CCN,0.2}$ and horizontal wind speed, and P value less than 0.05. The positive correlation has been previously seen over

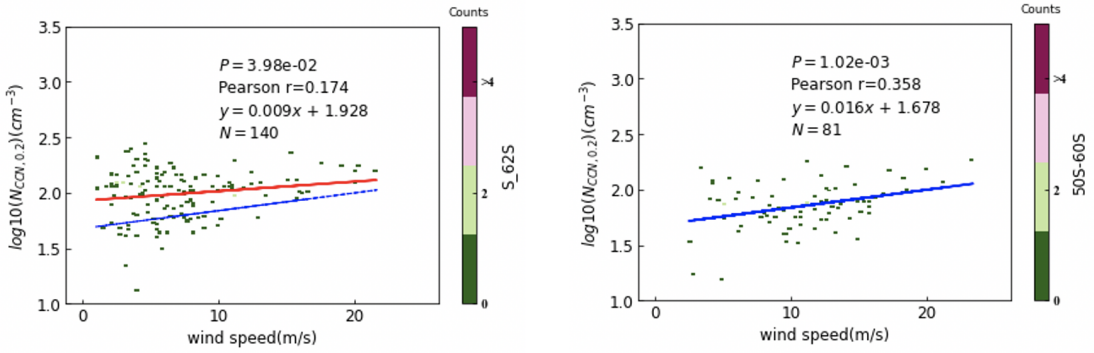

Figure 4.3: $N_{CCN,0.2}$ south of 62°S on the left and $N_{CCN,0.2}$ between 50°S and 60°S on the right as a function of wind speed after removal of ship stack. The blue line is the regression result derived with $N_{CCN,0.2}$ between 50°S and 60°S, it is copied in the left figure to compare with the red line that is derived with $N_{CCN,0.2}$ south of 62°S.

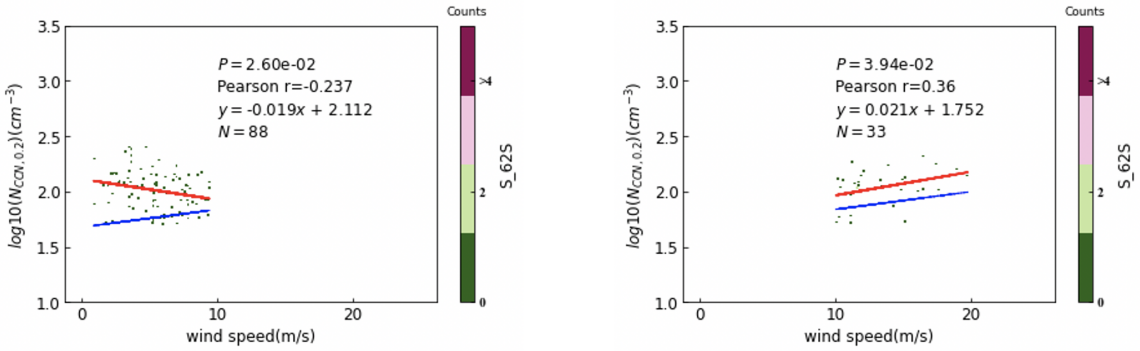

Figure 4.4: $N_{CCN,0.2}$ south of 62°S is negatively correlated to wind speed smaller than 10 $m\ s^{-1}$ (on the left) but positively correlated to wind speed larger than 10 $m\ s^{-1}$ (on the right). The blue line is the same to the blue line in Figure 4.3 and the red line is the fitting line for each figure.

the SO (Gras and Keywood 2017; Humphries et al. 2021). This result is consistent with a high ratio of primary aerosol serving as CCN, with the N_{CCN} increasing at high winds more wind-driven film drops generated at the ocean surface. The film drops here are refereed to as droplets with diameter ranging from tens of nanometers up to one micron-meterformed by the shatter of the film surrounding the bubble. However, Figure 4.4 shows a negative correlation between $N_{CCN,0.2}$ and horizontal wind smaller than 10 $m\ s^{-1}$. This negative correlation observed south of 62°S for boundary layer marine aerosol has not been discussed a lot and the reasons for the negative correlation are not well established. In-situ observations acquired during Southern Ocean Clouds, Radiation, Aerosol Transport Experimental Study (SOCRATES) at similar time to MARCUS by Sanchez et al. (2021) only cover the area north of 62°S, and found and found moderate correlation (r=0.53) between primary marine aerosol concentration and $CCN_{0.3}$ but no significant correlation between surface wind and $CCN_{0.3}$ Sanchez et al. (2021). Gras and Keywood (2017) studied the dependence of $CCN_{0.5}$ over the SO on wind speed using the data from Cape Grim, finding a negative correlation consistent with the MARCUS results. But, when their analysis was restricted to wind speed greater than 7 $m\ s^{-1}$ the correlation between $CCN_{0.5}$ and wind speed become positive during the summer. To explore the cause for the negative correlation, the accumulation mode aerosols were divided into different groups for studying the relationship with wind speed.

Figure 4.5 shows the correlation between the logarithm $CN_{700-1000}$ and wind speed on the left, and the logarithm CN_{60-100} and wind speed on the right. And Figure 4.6 shows the correlation between $CN_{100-350}$ and wind speed. The logarithm of $CN_{700-1000}$ is positively correlated to wind speed, with slope of 0.203 ($s \cdot m^{-1} cm^{-3}$) and P value smaller than 0.001, indicating the correlations are statistically significant. While the logarithm CN_{60-100} ($CN_{100-350}$) is negatively correlated with wind speed, with slope of -0.031 (-0.023) ($s \cdot m^{-1} cm^{-3}$) and P value smaller than 0.001. The positive correlation is consistent

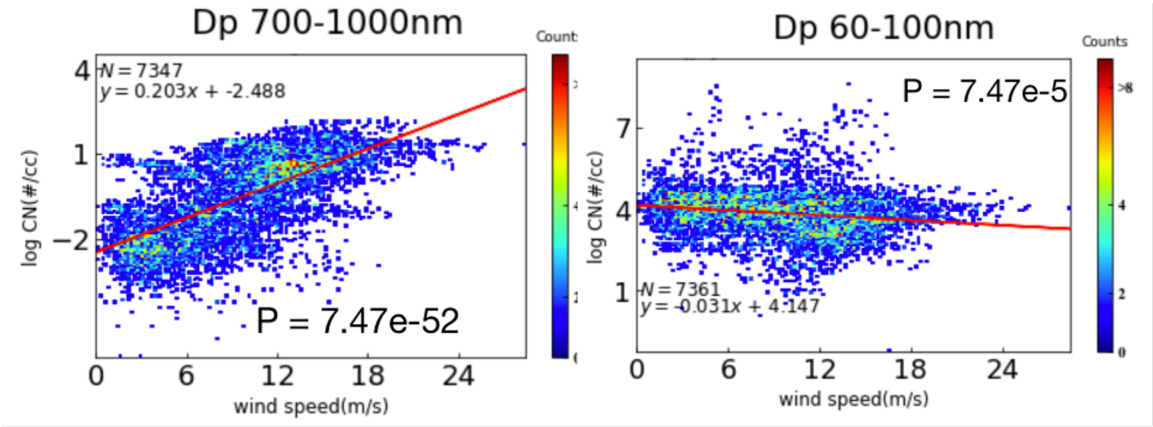

Figure 4.5: $CN_{700-1000}$ (left) and CN_{60-100} (right) as a function of wind speed

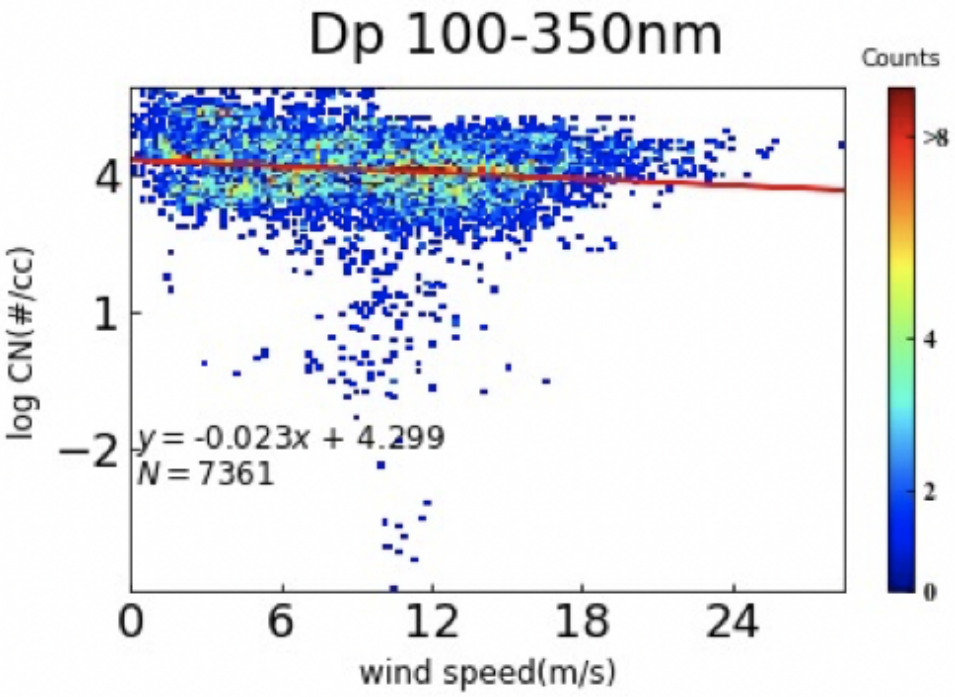

Figure 4.6: $CN_{100-350}$ as a function of wind speed

with previous theories of bubble and spray mechanisms of wind generation of sea salt particles and there are also numerical parameterizations used in models such as Gong (2003).

However the potential causes for the wind speed dependence for CN_{60-100} and $CN_{100-350}$ is less clear. Gras and Keywood (2017) previously showed that the aerosol concentration in 115–350 nm size range decreases with increasing wind speed over the SO in summer. They discussed the potential reasons for this observed trend related to competing processes of the source of aerosol through DMS (dimethyl sulfide) oxidation including heterogeneous reaction of SO_2 on sea salt spray, and sink of H_2SO_4 on super-micron sea salt during high winds. Zheng et al. (2018) included the CN_{60-100} together with other Aiken mode aerosols with D $<$100 nm in their analysis (referred as At), finding a negative wind speed dependence, while finding no significant dependence of $CN_{100-300}$ and wind speed. Zheng et al. (2018) mentioned that the observed negative relations between both $CN_{100-300}$ and CN_{60-100} and wind speed can be caused by the relatively minor contributions of SSA to At, and the negative correlation of $CN_{100-350}$ may also be due to the enhanced aerosols with diameter larger than 300 nm and thus enhanced coagulation loss for At. If the primary source of $CN_{100-350}$ is entrainment after cloud processing (Zheng et al. 2018), then with the same entrainment rate, high winds cause high transport speeds can also be a reason for the negative wind dependence. Since the CN_{60-100} together with $CN_{100-350}$ has one order of magnitude lower concentration than of aerosols with D $>$350 nm, the transformation associated with higher wind speeds may cause lower $CN_{60-1000}$ and CCN, especially south of 62°S where particles are smaller according to both the previous size distribution and AE analysis. This partly explains the negative wind speed dependence for $CCN_{0.2}$ south of 60°S.

In addition to the dependence on wind speed, the parcel history associated with the specific circulation pattern and air mass origin is another important meteorological control and is discussed in section 4.2.

4.2 Back trajectories

The Hybrid Single Particle Langranian Integrated Trajectories (Hysplit) model is used to derive 120-hour back trajectories with one hour time resolution. The GDAS reanalysis data are used as meteorology input (`ftp://arlftp.arlhq.noaa.gov/pub/archives/gdas1/`). The starting points are the location of AA at 25 meters above ground level (AGL), which is around the inlet of aerosol in AMF2.

Figure 4.7 shows the back trajectories of voyage between Hobart and Davis with starting points between 50°S and 60°S. For the whole MARCUS, 81% of the back trajectories with starting points between 50°S and 60°S have altitude below 1000 AGL meter in all the past five days and 76% below 500 AGL meter. Therefore most of the air mass comes from the west, transferred by the western flow in Ferrell Cell near the sea water.

According to the Figure 4.2, southern wind are dominant wind. Therefore we divide the current wind into west origin and east origin. Figure 4.9 (4.8) show the back trajectories start with western (eastern) flow of the same voyage as Figure 4.7 but with starting points south of 62°S. There are in total 95% of air mass come from altitude higher than 1000 AGL meter, unsurprisingly above the Antarctic continent. Since the unit is in AGL meter, the Antarctic topography may not affect the absolute value of altitude in this analysis. Since the air mass of aerosols south of 62°S has higher altitude, they are originated further away from the ocean which serves as the direct source of ocean-driven aerosols.

4.3 Sea ice

Figure 4.11 shows the change of sea ice scale as a function of latitude for a scale from 1 to 4. The AA first encounters with sea ice at 60-61°S, the sea ice scale largely increased south of 62°S, with some full scale sea ice conditions at 67°S and 63°S as shown by the third quartile. Also, there are also times when pure open water exist even at high latitude as 68°S.

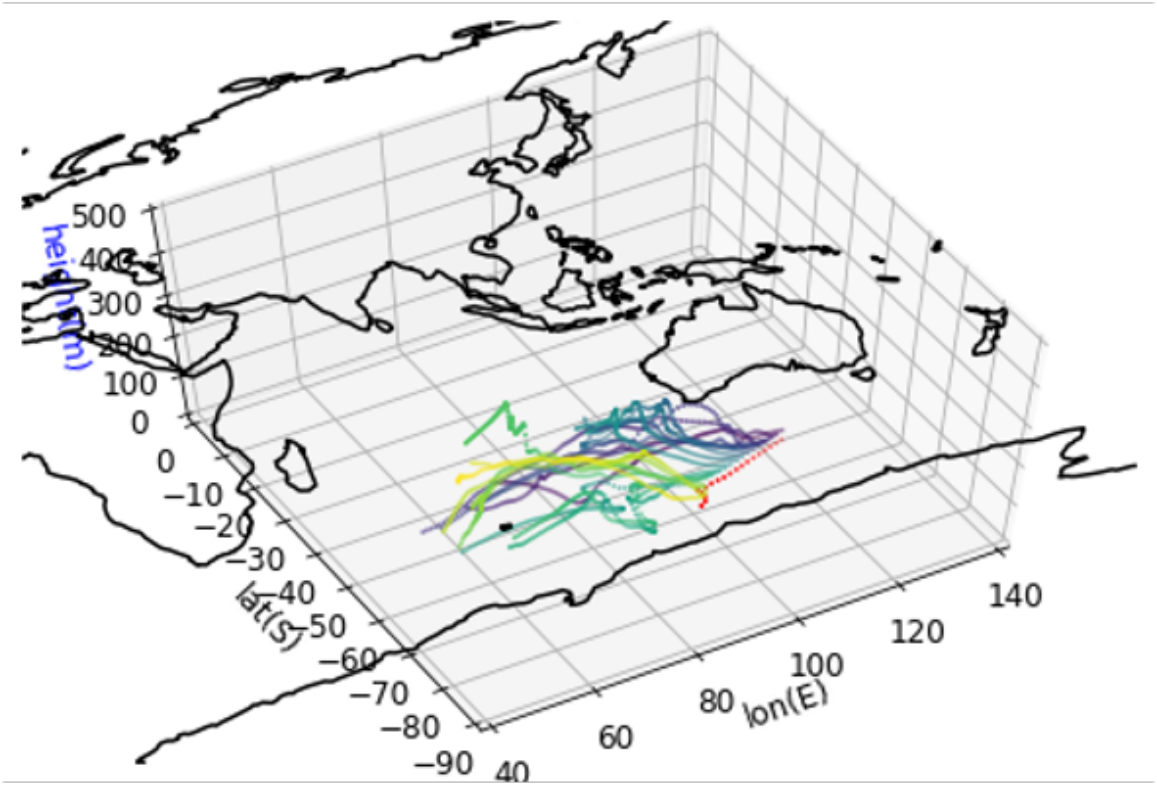

Figure 4.7: Spatial distribution of Hysplit back trajectory overlapped on map between 50°S and 60°S, each color is one 120-hour simulation with the AA location as the starting point marked as red scatter on the plot. Altitude in AGL meter. Figure has been rotated for better visualization.

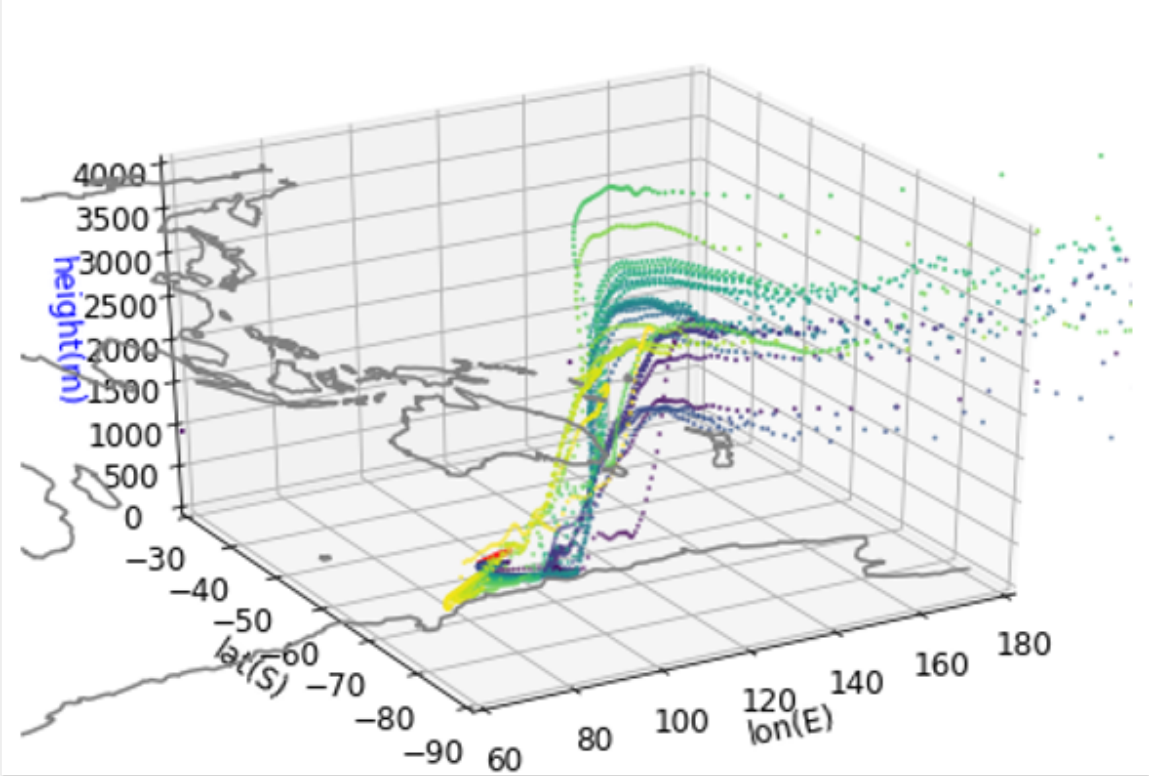

Figure 4.8: Spatial distribution of Hysplit back trajectory overlapped on map for concurrent east wind south of 62°S, each color is one 120-hour simulation with the AA location as the starting point marked as red scatter on the plot. Altitude in AGL meter. Figure has been rotated for better visualization.

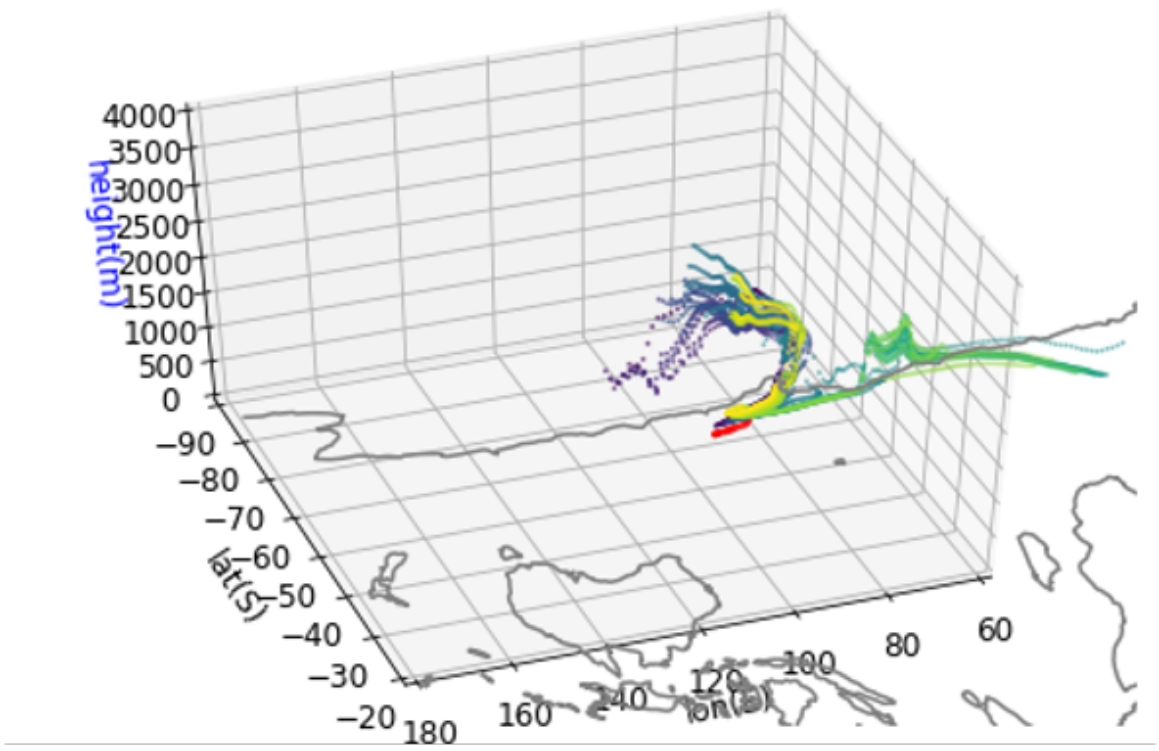

Figure 4.9: Spatial distribution of Hysplit back trajectory overlapped on map for concurrent west wind south of 62°S, each color is one 120-hour simulation with the AA location as the starting point marked as red scatter on the plot. Altitude in AGL meter. Figure has been rotated for better visualization.

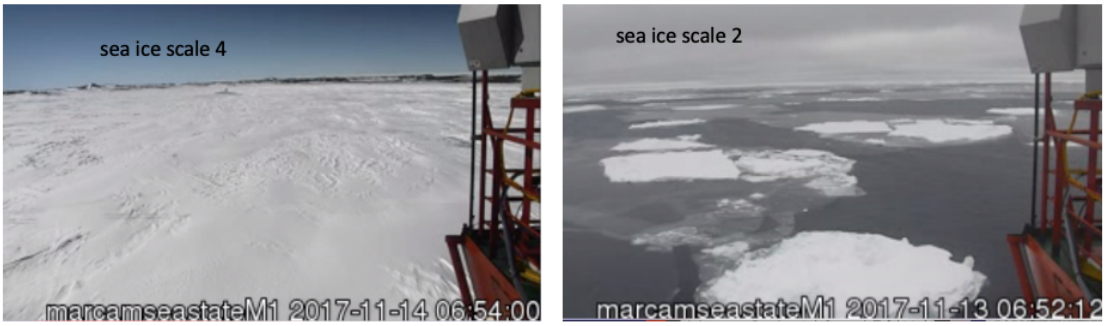

Figure 4.10: Sea ice scale observed from the sea state monitor on board. The left figure shows the time when sea ice fully covered the water and sea ice state defined as 4. The fight figure shows a time with only floating and scattered sea ice and its sea ice state is defined as 2.

As shown in Figure 3.1, south of 60°S, the $N_{CCN,0.2}$ and $N_{CCN,0.5}$ variability overall is larger than that between 50°S and 60°S. This includes both the variability at each latitude bin and the variation of $N_{CCN,0.2}$ ($N_{CCN,0.5}$) median value between latitudes. The average interquartile range south of 60°S is 35% (18%) larger than that between 50°S and 60°S, and the standard deviation of median $N_{CCN,0.2}$ ($N_{CCN,0.5}$) between latitudes is 46% (85%) larger. The variability at each bin can be explained by different scale of sea ice state during the MARCUS from spring to summer south of 60°S since every traction only pass one latitude once. This is consistent with the high variability of sea ice scale south of 60°S on Figure 3.1. The other variability between latitude can also be associated to sea ice for its influence on both primary and secondary ocean-driven aerosol. Primary aerosols as sea salt and organic aerosols driven by winds are restrained when the surface is covered by ice (Rinaldi et al. 2011). Secondary aerosols on the other hand can be affected by processes such as the release of DMS from ocean to the surface. The SO serves as a cold but highly productive region in the world especially near the Antarctic coast where the deep water is upwelled into the SO surface with phytoplankton (Deppeler and Davidson 2017). These phytokon blooms together with sea ice melting and coverage condition can influence the biognenic aerosol

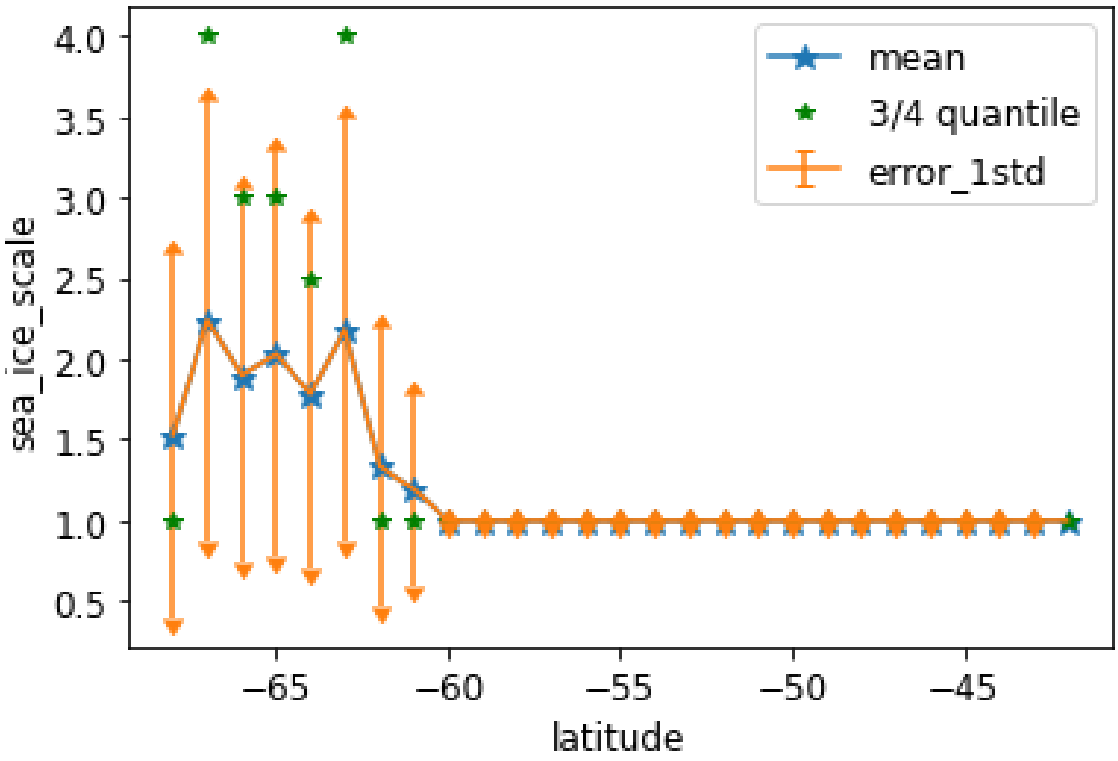

Figure 4.11: Sea ice degree as a function of latitude manually detected with sea state monitor camera. Definition of sea ice scale are defined as follows: Scale 4 is fully covered by sea ice and scale 1 is pure open water, Scale 3 in between is when floating scattered sea ice shows up. Error bar plots one standard deviation, green stars stand for the third quartile and the blue star for mean values.

precursors and the following formation of secondary organic aerosol. These secondary sulfur-based aerosols with small diameter aggressively dominant the number of CCN south of 60°S and to a large extent explained this latitudinal variation.

Chapter 5

Conclusion and Discussion

This study analyzed data from the MARCUS field campaign with the objective of understanding the sources, sinks and meteorological controls of accumulation mode aerosols ($CN_{60-1000}$) and CCN. In order to use aerosol and CCN data acquired in ambient conditions, a novel machine learning (ML) algorithm was first developed to remove time periods contaminated by ship exhaust. Using the data after removing contaminated time periods, the aerosol number concentration, size distributions and properties such as hygroscopicity Growth Factor (GF) and aerosol optical property scattering Angstrom Exponent (α) were determined. It was shown that there were distinct differences in those properties depending on whether they were measured between 50°S and 60°S or south of 62°S. Meteorological controls such as air mass origins, horizontal wind speed and sea ice scale of aerosol properties were also identified. The principle conclusions of this study are as follow.

1. The new developed ML ship stack identification scheme used CO and O_3 as input, allowing the retention of 31% more ship-borne aerosol observations than did application of previous Median Absolute Deviations (MAD)-based scheme using CN and *CO* as input devised by Humphries et al. (2021).

2. Regardless of which algorithm was used, it was seen that there were larger $N_{CCN,0.2}$ south of 60 and smaller $N_{CCN,0.2}$ between 50°S and south of 60°. MAD results showed means of 125 cm^{-3} (south of 60°S) and 102 cm^{-3} (between 50°S and 60°S) and the ML algorithm showed means of 110 cm^{-3} and 83 cm^{-3} for the respective latitudes.

3. Differences in total aerosol concentrations derived from the UHSAS for observations between 50°S and south of 60°S and south of 60°S were also derived. As the latitude

decreased from between 50°S and south of 60°S to south of 60°S, the $CN_{100-350}$ becomes 47% less while $CN_{700-1000}$ becomes 32% higher. This trend of more smaller accumulation mode aerosols near the Antarctic plateau and more larger accumulation mode aerosols between 50°S and south of 60°S was confirmed from analysis of the size distributions.

4. The α measured at 450, 550 and 700 nm wavelength shows modes of 0.5 ($\alpha_{450-550}$), 0.8 ($\alpha_{450-700}$) and 1.0 ($\alpha_{550-700}$) between 50°S and 60°S, whereas modes of 1.1 ($\alpha_{450-550}$), 1.4 ($\alpha_{450-700}$) and 1.5 ($\alpha_{550-700}$) were noted south of 62°S. Since contributions of all-sized aerosols are represented in the measurement of α, this also includes effects of aerosols with D <60 nm. Thus, aerosols with D <350 nm dominated the total aerosol number for both latitude ranges, with the northern latitudes having a broader size distributions with more large aerosols, consistent with the generation of larger SSA aerosols generated by higher wind speeds.

5. Measurements of the hygroscopicity GF show that for particles with 50, 100, 200, 250 nm diameter, the modes were respectively 1.41, 1.42, 1.34 and 1.34 for data collected south of 60°, whereas for those between 50°S and 60°S, the modes were 1.30, 1.38, 1.49 and 1.67 respectively. The hygroscopicity GF represents the aerosol capability to absorb water vapour from the environment. For aerosols with D >200 nm, the GF is higher in northern latitudes, this is consistent with the generation of more sea salt aerosols by higher wind speeds. For aerosols with D >200 nm, the GF is higher in southern, this is consistent with the frequent generation of small sulfur-based aerosol south of 60°S, and small wind-driven organic aerosol between 50°S and south of 60°S.

6. 120-hour back trajectories conducted with the HYSPLIT model show that 76% of trajectories come from the west for ship locations between 50°S and 60°S have origins with altitude below 500 AGL and west, implying that a large portion of air

masses were transported near the sea surface by westerlies. On the other hand, for ship locations south of 60°S, 95% of the air masses had origins higher than 1 km AGL and latitudes less than 62°S, implying their origins were in upper air over the Antarctic continent.

7. It was shown that the wind speed affects $CCN_{0.2}$ differently in between 50°S and 60°S and south of 60°S. $N_{CCN,0.2}$ is positively correlated with the horizontal wind speed (significance level of 0.05) with a correlation coefficient 0.35 between 50°S and 60°S, while south of 60°S there is a statistically significant negative correlation with correlation coefficient -0.21.

8. Both CN_{60-100} and $CN_{100-350}$ were negatively correlated in a statistically significant sense with wind speed using all data collected during MARCUS with slope of -0.031 ($s \cdot m^{-1} cm^{-3}$) and -0.023 ($s \cdot m^{-1} cm^{-3}$) respectively, while the $CN_{700-1000}$ has a positive correlation with wind speed with a slope of 0.203 ($s \cdot m^{-1} cm^{-3}$).

This study used a unique ship-borne dataset acquired during the MARCUS to analyze the potential CCN or CCN-active aerosol over the SO. It captured the transfer of size distribution between 50°S and 60°S and south of 60°S and found the wind speed dependence of $N_{CCN,0.2}$ is different. According to the properties such as hygroscopicity GF, this can be caused by chemical composition but more importantly, might have different sources and sinks in the atmosphere. This study improved the understanding of CCN formation and transportation over the SO, potentially beneficial to the simulation of marine boundary layer aerosol as well as the cloud-aerosol interaction research.

However, detailed and quantitative study on aerosol sources and sinks south of 60°S are still terribly challenging for limited in-situ observations, sparse meteorology sites, less frequent passes of satellite, large satellite tilting angle and high cloud coverage ratio. Besides, the current operational chlorophyll a retrieval algorithm is not perfectly applicable for the SO because of its extensively high chlorophyll a concentration. The ocean productivity itself, the integrated effects of wave, sea ice melting and ocean productivity on CCN is hard

to quantify as well. In current global warming scenario, the increasing wind speed over the SO, increasing sea ice melting and their influence on marine boundary layer CCN can also be of interest for future research about CCN sources and sinks.

Bibliography

Alroe, J., and Coauthors, 2020: Marine productivity and synoptic meteorology drive summer-time variability in southern ocean aerosols. *Atmospheric Chemistry and Physics*, **20 (13)**, 8047–8062, doi:10.5194/acp-20-8047-2020, URL https://acp.copernicus.org/articles/20/8047/2020/.

Asmi, E., and Coauthors, 2010: Hygroscopicity and chemical composition of antarctic sub-micrometre aerosol particles and observations of new particle formation. *Atmospheric Chemistry and Physics*, **10 (9)**, 4253–4271, doi:10.5194/acp-10-4253-2010, URL https://acp.copernicus.org/articles/10/4253/2010/.

Assessment, A. M. S., 2009: Report. *Arctic Council, April*.

Ayers, G., and J. Gras, 1991: Seasonal relationship between cloud condensation nuclei and aerosol methanesulphonate in marine air. *Nature*, **353 (6347)**, 834–835.

Barman, N., B. Saha, R. Roy, S. Kundu, A. Borgohain, and P. Raju, 2019: Investigation of curvature effect of Ångström exponent to classify the aerosol types over the region of interest (88-98 e and 20-30 n). *Atmospheric Pollution Research*, **10 (2)**, 363–373, doi:https://doi.org/10.1016/j.apr.2018.09.002, URL https://www.sciencedirect.com/science/article/pii/S1309104218300722.

Barthel, S., I. Tegen, and R. Wolke, 2018: Do new sea spray aerosol source functions improve the results of a regional aerosol model? *Atmospheric Environment*, **198**, doi:10.1016/j.atmosenv.2018.10.016.

Bodas-Salcedo, A., P. G. Hill, K. Furtado, K. D. Williams, P. R. Field, J. C. Manners, P. Hyder, and S. Kato, 2016: Large contribution of supercooled liquid clouds to the solar radiation budget of the southern ocean. *Journal of Climate*, **29 (11)**, 4213 – 4228, doi:10.1175/JCLI-D-15-0564.1, URL https://journals.ametsoc.org/view/journals/clim/29/11/jcli-d-15-0564.1.xml.

Bodas-Salcedo, A., and Coauthors, 2014: Origins of the solar radiation biases over the southern ocean in cfmip2 models. *Journal of Climate*, **27 (1)**, 41 – 56, doi:10.1175/JCLI-D-13-00169.1, URL https://journals.ametsoc.org/view/journals/clim/27/1/jcli-d-13-00169.1.xml.

Chen, Q., T. Sherwen, M. Evans, and B. Alexander, 2018: Dms oxidation and sulfur aerosol formation in the marine troposphere: a focus on reactive halogen and multiphase chemistry. *Atmospheric Chemistry and Physics*, **18 (18)**, 13 617–13 637, doi:10.5194/acp-18-13617-2018, URL https://acp.copernicus.org/articles/18/13617/2018/.

Coakley, J. A., R. L. BERNSTEIN, and P. A. DURKEE, 1987: Effect of ship-stack effluents on cloud reflectivity. *Science*, **237 (4818)**, 1020–1022, doi:10.1126/science.237.4818.1020, URL https://science.sciencemag.org/content/237/4818/1020, https://science.sciencemag.org/content/237/4818/1020.full.pdf.

Deppeler, S. L., and A. T. Davidson, 2017: Southern ocean phytoplankton in a changing climate. *Frontiers in Marine Science*, **4**, 40, doi:10.3389/fmars.2017.00040, URL https://www.frontiersin.org/article/10.3389/fmars.2017.00040.

Derkani, M. H., and Coauthors, 2021: Wind, waves, and surface currents in the southern ocean: observations from the antarctic circumnavigation expedition. *Earth System Science Data*, **13 (3)**, 1189–1209, doi:10.5194/essd-13-1189-2021, URL https://essd.copernicus.org/articles/13/1189/2021/.

Ferrel, W., 1859: *The motions of fluids and solids relative to the earth's surface*. Runkle's Mathematical Monthly 1, 140-148, 210–16, 300–7, 366–73, 397–406 pp.

Flato, G., and Coauthors, 2013: *Evaluation of climate models*, 741–882. Cambridge University Press, Cambridge, UK, doi:10.1017/CBO9781107415324.020.

Fossum, K., and Coauthors, 2018: Summertime primary and secondary contributions to southern ocean cloud condensation nuclei. *Scientific Reports*, **8**, doi:10.1038/s41598-018-32047-4.

Gong, S. L., 2003: A parameterization of sea-salt aerosol source function for sub- and super-micron particles. *Global Biogeochemical Cycles*, **17 (4)**, doi:https://doi.org/10.1029/2003GB002079, URL https://agupubs.onlinelibrary.wiley.com/doi/abs/10.1029/2003GB002079, https://agupubs.onlinelibrary.wiley.com/doi/pdf/10.1029/2003GB002079.

Gras, J., 1995: Cn, ccn and particle size in southern ocean air at cape grim. *Atmospheric Research*, **35 (2)**, 233–251, doi:https://doi.org/10.1016/0169-8095(94)00021-5, URL https://www.sciencedirect.com/science/article/pii/0169809594000215.

Gras, J. L., and M. Keywood, 2017: Cloud condensation nuclei over the southern ocean: wind dependence and seasonal cycles. *Atmospheric Chemistry and Physics*, **17 (7)**, 4419–4432, doi:10.5194/acp-17-4419-2017, URL https://acp.copernicus.org/articles/17/4419/2017/.

Graßl, S., and C. Ritter, 2019: Properties of arctic aerosol based on sun photometer long-term measurements in ny-Ålesund, svalbard. *Remote Sensing*, **11 (11)**, doi:10.3390/rs11111362, URL https://www.mdpi.com/2072-4292/11/11/1362.

Hamilton, D. S., L. A. Lee, K. J. Pringle, C. L. Reddington, D. V. Spracklen, and K. S. Carslaw, 2014: Occurrence of pristine aerosol environments on a polluted planet. *Proceedings of the National Academy of Sciences*, **111 (52)**, 18 466–18 471, doi:10.1073/pnas.1415440111, URL https://www.pnas.org/content/111/52/18466, https://www.pnas.org/content/111/52/18466.full.pdf.

Hanley, K. E., S. E. Belcher, and P. P. Sullivan, 2010: A global climatology of wind-wave interaction. *J. Phys. Oceanogr.*, **40**, 1263–1282.

Hoose, C., J. E. Kristjánsson, T. Iversen, A. Kirkevåg, Seland, and A. Gettelman, 2009: Constraining cloud droplet number concentration in gcms suppresses the aerosol indirect effect. *Geophysical Research Letters*, **36 (12)**, doi:https://doi.org/10.1029/2009GL038568, URL https://agupubs.onlinelibrary.wiley.com/doi/abs/10.1029/2009GL038568, https://agupubs.onlinelibrary.wiley.com/doi/pdf/10.1029/2009GL038568.

Hoskins, B. J., and K. I. Hodges, 2005: A new perspective on southern hemisphere storm tracks. *Journal of Climate*, **18 (20)**, 4108 – 4129, doi:10.1175/JCLI3570.1, URL https://journals.ametsoc.org/view/journals/clim/18/20/jcli3570.1.xml.

Hu, X.-M., M. Xue, F. Kong, and H. Zhang, 2019: Meteorological conditions during an ozone episode in dallas-fort worth, texas, and impact of their modeling uncertainties on air quality prediction. *Journal of Geophysical Research: Atmospheres*, **124 (4)**, 1941–1961, doi:https://doi.org/10.1029/2018JD029791, URL https://agupubs.onlinelibrary.wiley.com/doi/abs/10.1029/2018JD029791, https://agupubs.onlinelibrary.wiley.com/doi/pdf/10.1029/2018JD029791.

Humphries, R. S., and Coauthors, 2015: Boundary layer new particle formation over east antarctic sea ice – possible hg-driven nucleation? *Atmospheric Chemistry and Physics*, **15 (23)**, 13 339–13 364, doi:10.5194/acp-15-13339-2015, URL https://acp.copernicus.org/articles/15/13339/2015/.

Humphries, R. S., and Coauthors, 2021: Southern ocean latitudinal gradients of cloud condensation nuclei. *Atmospheric Chemistry and Physics Discussions*, **2021**, 1–35, doi:10.5194/acp-2020-1246, URL https://acp.copernicus.org/preprints/acp-2020-1246/.

IPCC, 2013: *Climate Change 2013: The Physical Science Basis. Contribution of Working Group I to the Fifth Assessment Report of the Intergovernmental Panel on Climate Change*. Cambridge University Press, Cambridge, United Kingdom and New York, NY, USA, 1535 pp., doi:10.1017/CBO9781107415324, URL www.climatechange2013.org.

J, U., and S. Smith, 2020: Arm aos. Accessed on 2021-04-21, https://www.arm.gov/capabilities/instruments/aos.

Kuang, C., 2016a: Condensation particle counter instrument handbook. doi:10.2172/1245983, URL https://www.osti.gov/biblio/1245983.

Kuang, C., 2016b: Tsi model 3936 scanning mobility particle spectrometer instrument handbook. doi:10.2172/1245993, URL https://www.osti.gov/biblio/1245993.

Kyrouac, J., 2019: Aerosol observing system surface meteorology (aosmet) instrument handbook. doi:10.2172/1251423, URL https://www.osti.gov/biblio/1251423.

Lachlan-Cope, T., and Coauthors, 2020: On the annual variability of antarctic aerosol size distributions at halley research station. *Atmospheric Chemistry and Physics*, **20 (7)**, 4461–4476, doi:10.5194/acp-20-4461-2020, URL https://acp.copernicus.org/articles/20/4461/2020/.

Lang, F., Y. Huang, S. T. Siems, and M. J. Manton, 2018: Characteristics of the marine atmospheric boundary layer over the southern ocean in response to the synoptic forcing. *Journal of Geophysical Research: Atmospheres*, **123 (15)**, 7799–7820, doi:https://doi.org/10.1029/2018JD028700, URL https://agupubs.onlinelibrary.wiley.com/doi/abs/10.1029/2018JD028700, https://agupubs.onlinelibrary.wiley.com/doi/pdf/10.1029/2018JD028700.

Latham, J., and M. Smith, 1990: Effect on global warming of wind-dependent aerosol generation at the ocean surface. *Nature*, **347 (6291)**, 372–373.

Mace, G. G., 2010: Cloud properties and radiative forcing over the maritime storm tracks of the southern ocean and north atlantic derived from a-train. *Journal of Geophysical Research: Atmospheres*, **115 (D10)**, doi:https://doi.org/10.1029/2009JD012517, URL https://agupubs.onlinelibrary.wiley.com/doi/abs/10.1029/2009JD012517, https://agupubs.onlinelibrary.wiley.com/doi/pdf/10.1029/2009JD012517.

Massel, S. R., 2007: *Ocean waves breaking and marine aerosol fluxes*, Vol. 38. Springer Science & Business Media.

Mather, K., and G. S. Miller, 1966: Wind drainage off the high plateau of eastern antarctica. *Nature*, **209 (5020)**, 281–284, doi:10.1038/209281a0, URL https://doi.org/10.1038/209281a0.

McCoy, D. T., S. M. Burrows, R. Wood, D. P. Grosvenor, S. M. Elliott, P.-L. Ma, P. J. Rasch, and D. L. Hartmann, 2015: Natural aerosols explain seasonal and spatial patterns of southern ocean cloud albedo. **1 (6)**, doi:10.1126/sciadv.1500157.

McCoy, D. T., D. L. Hartmann, and D. P. Grosvenor, 2014: Observed southern ocean cloud properties and shortwave reflection. part ii: Phase changes and low cloud feedback. *Journal of Climate*, **27 (23)**, 8858 – 8868, doi:10.1175/JCLI-D-14-00288.1, URL https://journals.ametsoc.org/view/journals/clim/27/23/jcli-d-14-00288.1.xml.

McFarquhar, G. M., and Coauthors, 2021: Observations of clouds, aerosols, precipitation, and surface radiation over the southern ocean: An overview of capricorn, marcus, micre and socrates. *Bulletin of the American Meteorological Society*, 1 – 92, doi:10.1175/BAMS-D-20-0132.1, URL https://journals.ametsoc.org/view/journals/bams/aop/BAMS-D-20-0132.1/BAMS-D-20-0132.1.xml.

Murphy, D., and Coauthors, 1998: Influence of sea-salt on aerosol radiative properties in the southern ocean marine boundary layer. *Nature*, **392 (6671)**, 62–65.

Naud, C. M., J. F. Booth, and A. D. Del Genio, 2014: Evaluation of era-interim and merra cloudiness in the southern ocean. *J. Climate*, **27 (5)**, 2109–2124, doi:10.1175/JCLI-D-13-00432.1.

O'Dowd, C. D., and G. de Leeuw, 2007: Marine aerosol production: a review of the current knowledge. *Philosophical Transactions of the Royal Society A: Mathematical,*

Physical and Engineering Sciences, **365 (1856)**, 1753–1774, doi:10.1098/rsta.2007.2043, URL https://royalsocietypublishing.org/doi/abs/10.1098/rsta.2007.2043, https://royalsocietypublishing.org/doi/pdf/10.1098/rsta.2007.2043.

O'Dowd, C. D., M. H. Smith, I. E. Consterdine, and J. A. Lowe, 1997: Marine aerosol, sea-salt, and the marine sulphur cycle: a short review. *Atmospheric Environment*, **31 (1)**, 73–80, doi:https://doi.org/10.1016/S1352-2310(96)00106-9, URL https://www.sciencedirect.com/science/article/pii/S1352231096001069.

Pedregosa, F., and Coauthors, 2011: Scikit-learn: Machine learning in Python. *Journal of Machine Learning Research*, **12**, 2825–2830.

Posyniak, M., and K. Markowicz, 2009: Measurement of aerosol optical thickness over the atlantic ocean and in west antarctica, 2006–2007. *Acta Geophysica*, **57**, 494–508, doi:10.2478/s11600-009-0002-0.

Pruppacher, H. R., and J. D. Klett, 1997: *Microphysics of Clouds and Precipitation*. Kluwer Academic Publisher, ch.17 pp.

Quinn, P., and T. Bates, 2014: *Treatise on geochemistry,Second Edition*. Elsevier Pergamon, Oxford, UK; San Diego, CA, USA.

Quinn, P., D. Coffman, J. Johnson, L. Upchurch, and T. Bates, 2017: Small fraction of marine cloud condensation nuclei made up of sea spray aerosol. *Nature Geoscience*, **10 (9)**, 674–679.

Rinaldi, M., and Coauthors, 2011: Evidence of a natural marine source of oxalic acid and a possible link to glyoxal. *Journal of Geophysical Research: Atmospheres*, **116 (D16)**, doi:https://doi.org/10.1029/2011JD015659, URL https://agupubs.onlinelibrary.wiley.com/doi/abs/10.1029/2011JD015659, https://agupubs.onlinelibrary.wiley.com/doi/pdf/10.1029/2011JD015659.

Sanchez, K. J., and Coauthors, 2021: Measurement report: Cloud processes and the transport of biological emissions affect southern ocean particle and cloud condensation nuclei concentrations. *Atmospheric Chemistry and Physics*, **21 (5)**, 3427–3446, doi:10.5194/acp-21-3427-2021, URL https://acp.copernicus.org/articles/21/3427/2021/.

Schill, S., and Coauthors, 2015: The impact of aerosol particle mixing state on the hygroscopicity of sea spray aerosol. *ACS Central Science*, **1**, 132–141, doi:10.1021/acscentsci.5b00174.

Schmale, J., and Coauthors, 2019: Overview of the antarctic circumnavigation expedition: Study of preindustrial-like aerosols and their climate effects (ace-space). *Bulletin of the American Meteorological Society*, **100 (11)**, 2260 – 2283, doi:10.1175/BAMS-D-18-0187.1, URL https://journals.ametsoc.org/view/journals/bams/100/11/bams-d-18-0187.1.xml.

Simmonds, I., and K. Keay, 2000: Mean southern hemisphere extratropical cyclone behavior in the 40-year ncep–ncar reanalysis. *Journal of Climate*, **13 (5)**, 873 – 885, doi:10.1175/1520-0442(2000)013⟨0873:MSHECB⟩2.0.CO;2, URL https://journals.ametsoc.org/view/journals/clim/13/5/1520-0442_2000_013_0873_mshecb_2.0.co_2.xml.

Simmons, J. B., and Coauthors, 2021: Summer aerosol measurements over the east antarctic seasonal ice zone. *Atmospheric Chemistry and Physics*, **21 (12)**, 9497–9513, doi:10.5194/acp-21-9497-2021, URL https://acp.copernicus.org/articles/21/9497/2021/.

Simó, R., and J. Dachs, 2002: Global ocean emission of dimethylsulfide predicted from biogeophysical data. *Global Biogeochemical Cycles*, **16 (4)**, 26–1–26–10, doi:https://doi.org/10.1029/2001GB001829, URL https://agupubs.onlinelibrary.wiley.com/doi/abs/10.1029/2001GB001829, https://agupubs.onlinelibrary.wiley.com/doi/pdf/10.1029/2001GB001829.

Sinha, P., and Coauthors, 2003: Emissions of trace gases and particles from savanna fires in southern africa. *Journal of Geophysical Research*, **108**, doi:10.1029/2002JD002325.

Svenningsson, B., and Coauthors, 2006: Hygroscopic growth and critical supersaturations for mixed aerosol particles of inorganic and organic compounds of atmospheric relevance. *Atmospheric Chemistry and Physics*, **6 (7)**, 1937–1952, doi:10.5194/acp-6-1937-2006, URL https://acp.copernicus.org/articles/6/1937/2006/.

Tang, G., and Coauthors, 2021: Bypassing the nox titration trap in ozone pollution control in beijing. *Atmospheric Research*, **249**, 105 333, doi:https://doi.org/10.1016/j.atmosres.2020.105333, URL https://www.sciencedirect.com/science/article/pii/S0169809520312709.

Turner, D. R., I.-M. Hassellöv, E. Ytreberg, and A. Rutgersson, 2017: Shipping and the environment: Smokestack emissions, scrubbers and unregulated oceanic consequences. *Elementa: Science of the Anthropocene*, **5**, doi:10.1525/elementa.167, URL https://doi.org/10.1525/elementa.167, 45, https://online.ucpress.edu/elementa/article-pdf/doi/10.1525/elementa.167/430063/167-3631-1-pb.pdf.

Twohy, C. H., and Coauthors, 2021: Cloud-nucleating particles over the southern ocean in a changing climate. *Earth's Future*, **9 (3)**, e2020EF001 673, doi:https://doi.org/10.1029/2020EF001673, URL https://agupubs.onlinelibrary.wiley.com/doi/abs/10.1029/2020EF001673, e2020EF001673 2020EF001673, https://agupubs.onlinelibrary.wiley.com/doi/pdf/10.1029/2020EF001673.

Uetake, J., T. C. J. Hill, K. A. Moore, P. J. DeMott, A. Protat, and S. M. Kreidenweis, 2020: Airborne bacteria confirm the pristine nature of the southern ocean boundary layer. *Proceedings of the National Academy of Sciences*, **117 (24)**, 13 275–13 282, doi:10.1073/pnas.2000134117, URL https://www.pnas.org/content/117/24/13275, https://www.pnas.org/content/117/24/13275.full.pdf.

Uin, J., 2016a: 3002 humidified tandem differential mobility analyzer instrument handbook. doi:10.2172/1251403, URL https://www.osti.gov/biblio/1251403.

Uin, J., 2016b: Cloud condensation nuclei particle counter (ccn) instrument handbook. doi:10.2172/1251411, URL https://www.osti.gov/biblio/1251411.

Uin, J., 2016c: Integrating nephelometer instrument handbook. doi:10.2172/1246075, URL https://www.osti.gov/biblio/1246075.

Uin, J., 2016d: Ultra-high-sensitivity aerosol spectrometer (uhsas) instrument handbook. doi:10.2172/1251410, URL https://www.osti.gov/biblio/1251410.

Uin, J., and Coauthors, 2019: Atmospheric radiation measurement (arm) aerosol observing systems (aos) for surface-based in situ atmospheric aerosol and trace gas measurements. *Journal of Atmospheric and Oceanic Technology*, **36 (12)**, 2429 – 2447, doi:10.1175/JTECH-D-19-0077.1, URL https://journals.ametsoc.org/view/journals/atot/36/12/jtech-d-19-0077.1.xml.

Williams, J., M. de Reus, R. Krejci, H. Fischer, and J. Ström, 2002: Application of the variability-size relationship to atmospheric aerosol studies: estimating aerosol lifetimes and ages. *Atmospheric Chemistry and Physics*, **2 (2)**, 133–145, doi:10.5194/acp-2-133-2002, URL https://acp.copernicus.org/articles/2/133/2002/.

Xu, W., J. Ovadnevaite, K. N. Fossum, C. Lin, R.-J. Huang, C. O'Dowd, and D. Ceburnis, 2020: Aerosol hygroscopicity and its link to chemical composition in the coastal atmosphere of mace head: marine and continental air masses. *Atmospheric Chemistry and Physics*, **20 (6)**, 3777–3791, doi:10.5194/acp-20-3777-2020, URL https://acp.copernicus.org/articles/20/3777/2020/.

Yuan, X., J. Patoux, and C. Li, 2009: Satellite-based midlatitude cyclone statistics over the southern ocean: 2. tracks and surface fluxes. *Journal of Geophysical Research: Atmospheres*, **114 (D4)**, doi:https://doi.org/10.1029/2008JD010874, URL https://agupubs.onlinelibrary.wiley.com/doi/abs/10.1029/2008JD010874, https://agupubs.onlinelibrary.wiley.com/doi/pdf/10.1029/2008JD010874.

Zheng, G., and Coauthors, 2018: Marine boundary layer aerosol in the eastern north atlantic: seasonal variations and key controlling processes. *Atmospheric Chemistry and Physics*, **18 (23)**, 17 615–17 635, doi:10.5194/acp-18-17615-2018, URL https://acp.copernicus.org/articles/18/17615/2018/.